

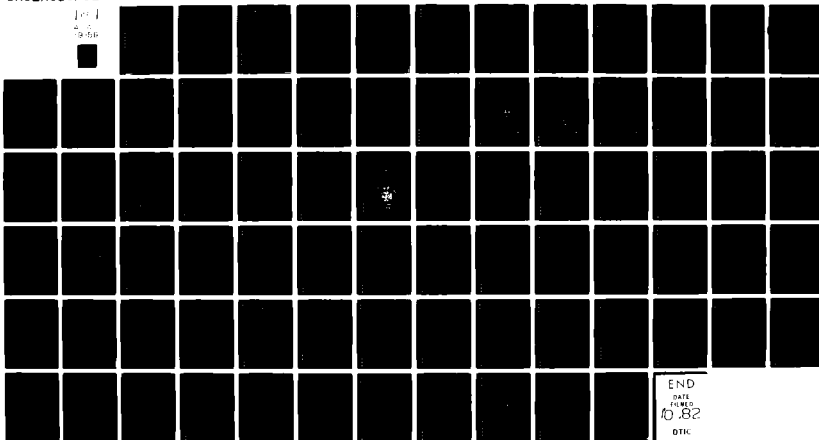
AD-A119 356

CTI-CRYOGENICS WALTHAM MA F/G 13/1
CLOSED CYCLE CRYOCOOLER FOR LOW TEMPERATURE ELECTRONIC CIRCUITS--ETC(U)
AUG 82 F W PIRTLE N00014-81-C-0525

UNCLASSIFIED

NL

1 of 1
9-56



END
DATE
FILMED
10-82
DTIC

(12)

CTI-CRYOGENICS

AD A119356

DTIC FILE COPY

DTIC
SEP 20 1982
A

This document has been approved
for public release and sale; its
distribution is unlimited.

HELIX
A Helix Company

82 09 08 019

NR. 410-002

CLOSED CYCLE CRYOCOOLER
FOR LOW TEMPERATURE ELECTRONIC CIRCUITS

PHASE II: PRELIMINARY DESIGN
CONTRACT N00014-81-C-0525

CTI-CRYOGENICS
A Division of Helix Technology Corporation
Kelvin Park
Waltham, MA 02254

Final Report
August 1982

Submitted to:

Office of Naval Research
Department of the Navy
800 N. Quincy Street
Arlington, Virginia 22217

DTIC
ELECTE
SEP 20 1982
A

This document has been approved
for public release and sale; its
distribution is unlimited.

SECURITY CLASSIFICATION OF THIS PAGE (When Data Entered)

REPORT DOCUMENTATION PAGE		READ INSTRUCTIONS BEFORE COMPLETING FORM
1. REPORT NUMBER	2. GOVT ACCESSION NO. AD-A119356	3. RECIPIENT'S CATALOG NUMBER
4. TITLE (and Subtitle) CLOSED CYCLE CRYOCOOLER FOR LOW TEMPERATURE ELECTRONIC CIRCUITS PHASE II: PRELIMINARY DESIGN		5. TYPE OF REPORT & PERIOD COVERED FINAL REPORT 15 May 1981 thru 30 Sept. 81
7. AUTHOR(s) F. William Pirtle		6. CONTRACT OR GRANT NUMBER(s) N00014-81-C-0525
9. PERFORMING ORGANIZATION NAME AND ADDRESS CTI-CRYOGENICS A Division of Helix Technology Corporation Kelvin Park, Waltham, MA 02254		10. PROGRAM ELEMENT, PROJECT, TASK AREA & WORK UNIT NUMBERS
11. CONTROLLING OFFICE NAME AND ADDRESS Office of Naval Research, Department of the Navy 800 N. Quincy Street Arlington, Virginia 22217		12. REPORT DATE August 1982
14. MONITORING AGENCY NAME & ADDRESS (if different from Controlling Office)		13. NUMBER OF PAGES
		15. SECURITY CLASS. (of this report) Unclassified
		15a. DECLASSIFICATION/DOWNGRADING SCHEDULE
16. DISTRIBUTION STATEMENT (of this Report)		
<div style="border: 1px solid black; padding: 5px; text-align: center;"> This document has been approved for public release and sale; its distribution is unlimited. </div>		
17. DISTRIBUTION STATEMENT (of the abstract entered in Block 20, if different from Report)		
18. SUPPLEMENTARY NOTES		
19. KEY WORDS (Continue on reverse side if necessary and identify by block number) Ceramic, Cryocooler, Cryogenic, Low Magnetic Signature, Macor, Mechanical Design, Preliminary Design, Refrigerator, Regenerative, Stirling Cycle		
20. ABSTRACT (Continue on reverse side if necessary and identify by block number) This study program was conducted under Office of Naval Research contract N00014-81-C-0525 to develop a preliminary design of a small, low power, very low magnetic signature, lightweight, efficient closed cycle cryocooler suitable for use with superconductive and other low temperature electronics circuits. The preliminary design is directly based on the results of the Phase I concept study (contract N00014-80-C-0465). The cryocooler is to		

produce 50 milliwatts at 10K or less with electrical input power not to exceed 250 watts. Temperature fluctuations at the electronics of ± 0.01 K or less are required. The zero load temperature is to be 8K or less. Cooldown time is to be approximately 24 hours or less with 300 grams of electronics attached. The weight goal is 4540 grams including 300 grams of electronics. The magnetic field at the cold volume is to approach 10^6 gauss or less with a goal of 10^{-8} gauss for all frequencies between zero and several hundred kilohertz. Maximum cold volume flexing or rotation is to approach 10^{-5} radians with a goal of 10^{-7} radians at frequencies harmonically related to the driving frequency.

The impact of electronics interface requirements was studied. Electronics package volumes of 4 cm diameter by 15 cm long and 10 cm diameter by 10 cm long were considered. A thermodynamic optimization study was performed. An input power of 205 watts will be required using the 4 cm by 15 cm electronic volume. The magnetic susceptibility of MACORTM was investigated with the objectives of determining if standard MACORTM will produce an acceptable magnetic signature and if a special low magnetic susceptibility composition can be formulated. Results indicate that standard MACORTM has acceptable magnetic properties. The permeation of helium gas through MACORTM was experimentally investigated. Methods of reducing helium permeation were explored. A magnetic signature analysis was performed. A magnetic shield system was developed to attenuate the motor and compressor magnetic signature.

The resulting preliminary design satisfies the specifications for thermal capacity, input power, temperature stability, zero load temperature, and approximate cooldown time. Weight and volume goals are exceeded primarily because of the shield system needed to satisfy the magnetic signature requirement.

FOREWORD

This report is the final technical document describing the work accomplished under Office of Naval Research Contract N00014-81-C-0525. The report describes the thermodynamic and mechanical preliminary design of the closed cycle cryo-cooler for low temperature electronic circuits based on the results of the Phase I study (Contract N00014-80-C-0465).

Technical contributions have been made by:

Dr. Peter J. Kerney, CTI-CRYOGENICS, Program Manager

Dr. F. William Pirtle, CTI-CRYOGENICS, Program Engineer

Peter K. Bertsch, CTI-CRYOGENICS, Advanced Development Engineer

Corning Glass Works, Consultants for MACORTM properties

Arthur D. Little, Inc., Consultants for magnetic signature

This report was prepared by Dr. F. William Pirtle, Program Engineer.



Acceptance For	
DTIC	<input checked="checked" type="checkbox"/>
DTIC	<input type="checkbox"/>
DTIC	<input type="checkbox"/>
<i>Added on file</i>	
By	
Distribution	
Availability Codes	
Avail. and/or	
Dist	Special
A	

TABLE OF CONTENTS

<u>SECTION</u>		<u>PAGE</u>
I.	ABSTRACT.	1x
II.	INTRODUCTION.	1
	Purpose.	2
	Scope.	2
	Design Requirements.	2
III.	THERMODYNAMIC DESIGN.	5
	Description of Analysis.	5
	Interface Condition Study.	6
	Thermodynamic Optimization	8
	Thermodynamic Results.	13
	Low Temperature Capacity	13
	Cooldown Time.	18
IV.	MECHANICAL DESIGN	20
	General.	20
	Major Design Features and Tradeoffs.	22
V.	MACOR TM MAGNETIC SUSCEPTIBILITY REDUCTION	24
	conclusions From Magnetic Susceptibility and Property Study.	24
VI.	MACOR TM HELIUM PERMEATION STUDY	26
	Introduction	26
	Results.	27
	Discussion	27
VII.	VIBRATION ANALYSIS WITH MAGNETIC SIGNATURE.	29
	Angular Movement	29
	Pressure Wave Stretching	31
	Displacer Stroking	32
VIII.	DRIVE MOTOR MAGNETIC SIGNATURE ANALYSIS	33
	Introduction	33
	Conclusions Based on Magnetic Signature Analysis	35
IX.	CONCLUSIONS	36
X.	APPENDIX A, MACOR TM MAGNETIC SUSCEPTIBILITY AND PROPERTY STUDY	37
	Composition.	37
	Properties	38

TABLE OF CONTENTS

<u>SECTION</u>		<u>PAGE</u>
XI.	APPENDIX B, MAGNETIC SIGNATURE DEVELOPMENT	
	Rotor Poles	48
	Field Inside Shielding Can	49
	Can Shielding Factors.	54
	Estimation of Fields at the End of the Cold Finger	61

LIST OF FIGURES

<u>FIGURE</u>	<u>TITLE</u>	<u>PAGE</u>
1.	Small MACOR TM Concept, Diameter Study	9
2.	Small MACOR TM Concept, Stage Length Parameter Study	10
3.	Small MACOR TM Concept, Gap Thickness Parameter Study.	11
4.	Small MACOR TM Study, Input Power vs. Minimum Pressure	12
5.	Small MACOR TM Study, Input Power vs. Maximum Pressure	14
6.	Small MACOR TM Study, Input Power vs. Stroke Length.	15
7.	Preliminary Design Capacity Below 10 K.	17
8.	Preliminary Design, Cooldown Curves For Each Stage.	19
9.	Preliminary Mechanical Design	21
10.	Model for Angular Vibration of Electronics.	30
11.	Field at Baseplate.	64
12.	Concentric Shield Assembly.	65
13.	Shield Effectiveness.	66

LIST OF TABLES

<u>TABLE</u>	<u>TITLE</u>	<u>PAGE</u>
1	INTERFACE THERMAL LOADS	7
2	SYSTEM WEIGHT AND VOLUME.	7
3	PRELIMINARY DESIGN PARAMETERS	16
4	HELIUM PERMEATION RATES	28
5	CHEMICAL ANALYSIS OF EXPERIMENTAL COMPOSITION A	42
6	MAGNETIC SUSCEPTIBILITY DATA.	43
7	CALCULATED VALUES OF DIAMAGNETIC AND PARAMAGNETIC SUSCEPTIBILITY.	44
8	STRENGTH MEASUREMENTS ON EXPERIMENTAL RESULTS	45
9	THERMAL EXPANSION COEFFICIENTS.	46
10	SPECIFIC HEAT OF MACOR TM	47
11	COORDINATES OF THE ROTOR POLES.	63

NOMENCLATURE

<u>Symbol</u>	<u>Definition</u>	<u>Unit</u>
A	Area	cm ²
a	4th stage displacer radius	cm
b	Cylinder length	cm
D	Diameter (of stage)	cm
G	Gap thickness (radial)	cm
G	Gradient in Earth's Magnetic Field	gauss/kilometer
H	Magnetic field	gauss
H ₀	Earth's Magnetic Field	gauss
ij	Effect of stage i	
	Quantity on stage j	
I ₀	Moment of inertia	in lb sec ²
J	Surface current density	amp/cm ²
K	Diffusion constant	std cc mm/sec cm ² cm Hg
		Hg
L	Length (of stage)	cm
M	Magnetic moment per unit volume	amp/cm
M.I.	Machinability index	
P	Pressure	atm (PSIA)
P	Pole strength	gaussian units
ΔP	Pressure difference	cm of Hg
Q	Helium diffusion rate	std cc/sec
r ₀	Radius	cm
S	Number of strokes (in machinability determination)	
T	Temperature	K
T	Torque	lb in
T ₀	Torque amplitude	lb in
T ₁ , T ₂	Depths at ends of machinability sample cut	
Δx	Wall thickness	mm
α	Stroke	cm
μ	Shielding factor	
μ ₀	Diamagnetic susceptibility	cm ³ /g
μ'	Paramagnetic susceptibility	cm ³ /g

NOMENCLATURE

Symbol

Definition

Unit

θ

Angle

radians

χ

Magnetic susceptibility

z

Distance from the mean position of the
end of the displacer

cm

I. ABSTRACT

This study program was conducted under Office of Naval Research contract N00014-81-C-0525 to develop a preliminary design of a small, low power, very low magnetic signature, lightweight, efficient closed cycle cryocooler suitable for use with superconductive and other low temperature electronic circuits. The preliminary design is directly based on the results of the Phase I concept study (contract N00014-80-C-0465). The cryocooler is to produce 50 milliwatts at 10 K or less with electrical input power not to exceed 250 watts. Temperature fluctuations at the electronics of ± 0.01 K or less are required. The zero load temperature is to be 8 K or less. Cooldown time is to be approximately 24 hours or less with 300 grams of electronics attached. The weight goal is 4540 grams including 300 grams of electronics. The magnetic field at the cold volume is to approach 10^{-6} gauss or less with a goal of 10^{-8} gauss for all frequencies between zero and several hundred kilohertz. Maximum cold volume flexing or rotation is to approach 10^{-5} radians with a goal of 10^{-7} radians at frequencies harmonically related to the driving frequency.

The impact of electronics interface requirements was studied. Electronics package volumes of 4 cm diameter by 15 cm long and 10 cm diameter by 10 cm long were considered. A thermodynamic optimization study was performed. An input power of 205 watts will be required using the 4 cm by 15 cm electronics volume. The magnetic susceptibility of MACORTM was investigated with the objectives of determining if standard MACORTM will produce an acceptable magnetic signature and if a special low magnetic susceptibility composition can be formulated. Results indicate that standard MACORTM has acceptable magnetic properties. The permeation of helium gas through MACORTM was experimentally investigated. Methods of reducing helium permeation were explored. A magnetic signature analysis was performed. A magnetic shield system was developed to attenuate the motor and compressor magnetic signature.

The resulting preliminary design satisfies the specifications for thermal capacity, input power, temperature stability, zero load temperature, and approximate cooldown time. Weight and volume goals are exceeded primarily because of the shield system needed to satisfy the magnetic signature requirement.

II. INTRODUCTION

The application of superconductivity to electronic instruments offers many advantages. Among these are reduced power requirements, size, and weight. In order to fully achieve these advantages the power requirements, size, and weight of the refrigeration system necessary to support the electronics must also be reduced.

The Phase I concept study of this program, Contract N00014-80-C-0465 (Final Report Nov. 1980), successfully addressed the question of whether the refrigeration system (cryocooler) was conceptually feasible to apply to superconductive electronic devices.

State of the art superconducting magnetometers are sensitive to magnetic signals on the order of 10^{-11} G Hz^{-1/2} and gradiometers are sensitive to 10^{-12} G cm⁻¹ Hz^{-1/2}. The magnetic noise induced by the cryocooler at the electronics within the effective bandwidth must be compatible with these magnitudes. Materials used in the cryocooler construction should consequently be non-ferromagnetic and electrically insulating because movement of ferromagnetic materials in the Earth's magnetic field of 0.5 gauss produces a magnetic disturbance large enough to mask the intended measurement. Movement of an electrical conductor in the Earth's field causes electrical current generation which is also a source of magnetic disturbance.

The Phase I primary concept was partially constructed of a machineable glass ceramic (MACORTM) produced by Corning Glass Works. MACORTM was found to be thermodynamically acceptable; however, some properties, i.e., magnetic susceptibility, thermal conductivity and specific heat, needed further clarification. Accordingly, CTI-CRYOGENICS enlisted Corning Glass Works to evaluate these properties in more detail.

Vibration and magnetic signature characteristics have been evaluated in developing the preliminary design. CTI-CRYOGENICS team members have been assisted by Arthur D. Little consultants in this evaluation.

Purpose

The purpose of this effort is to develop a preliminary design of the optimum cryogenic refrigeration system for application to superconductive electronics based on the direct results of the Phase I concept study.

Scope

The scope of the program includes the following:

- Develop a preliminary detailed design of the Phase I cryocooler concept as modified by the interface requirement study. The design shall include the results of the thermodynamic optimization, helium permeation reduction, vibration and magnetic susceptibility reduction efforts.
- Further optimize the thermodynamic performance of the concept.
- Perform a material property evaluation for MACORTM.
- Determine the most effective way to eliminate helium permeation through MACORTM.
- Perform a vibration and magnetic signature analysis of the cryocooler preliminary design.

Design Requirements

The cryocooler must satisfy the following design requirements from the statement of work:

- Two electronics volumes, 4 cm diameter by 15 cm long and 10 cm diameter by 10 cm long, are to be considered with regard to the impact on the cryocooler input power, size, and cooldown time.
- The cryocooler shall have reserve cooling capacity of 20 milliwatts at 10 K and a maximum no load temperature of 8 K. The nominal capacity is 50 milliwatts at 10 K.

- The impact of three coaxial leads shall be included. Each lead typically contains a uniform tube of UT85 stainless steel (0.0865-inch OD and 0.0658-inch ID), and a precision tube of JT 50085 beryllium copper or equivalent (0.0201-inch diameter). The annular space between the conductors is teflon. The DC resistance of each coaxial lead is greater than 0.1 ohms.
- Temperature stability of operation shall be ± 0.01 K.
- The system weight goal (including 300 grams of electronics) is less than 4.54 kg. The corresponding volume goal is 9800 cm³.
- The cooldown time goal is 24 hours.
- The maximum input power is 250 watts.
- No active pumping of the vacuum space is allowed.

As a result of a design review on 21 September 1981, the following information was provided to assist in the preparation of the Phase II preliminary design:

- The design should use a cold volume of 4 cm diameter by 15 cm long.
- The cooldown time for 300 grams of electronics is 24 hours subject to the constraint that the electrical input power not exceed 250 watts. Using the design resulting from the 24 hour cooldown specification, the cooldown times for 150 grams of electronics and no electronics is to be estimated.
- An integral (instead of split) design is preferred
- Heat generated at room temperature should be removed by ambient air cooling or by conduction through the mechanical support structure.
- 400 Hz input power is available.

- The stray magnetic field at the point where the cold volume is connected to the cold station of the cryocooler should approach 10^{-6} gauss peak to peak with a goal of 10^{-8} gauss peak to peak for all frequencies between zero and several hundred kilohertz.
- The maximum rotation or flexing of the cold volume relative to some external reference frame should approach 10^{-5} radians peak to peak with a goal of 10^{-7} radians at frequencies harmonically related to the drive frequency and much lower at other frequencies below several kilohertz.

III. THERMODYNAMIC DESIGN

Description of Analysis

The thermodynamic design has included studies in the following areas:

- Study of 4 cm diameter x 15 cm and 10 cm diameter x 10 cm electronics volumes
 - input power
 - conduction lead loss
 - radiation losses
 - weight and volume
- Thermodynamic optimization (constant stage capacity)
 - stage diameter
 - stage length
 - gap
 - minimum pressure
 - maximum pressure
 - cycle rate
 - stroke
- Capacity at temperatures less than 10 K.
- Cooldown time
 - specification 24 hour design for 300 grams of electronics
 - estimate of time to cool 150 grams
 - estimate of cooldown time with no electronics

Interface Condition Study

The Phase I concepts were based on an electronics volume of 0.89 cm diameter by 2.54 cm long. Phase II specifications include consideration of two electronics volumes, both with 300 grams of electronics. The volumes have been specified in the design requirements. The interface study has included the effects of the coax electrical lead losses and radiation losses including two radiation shields attached to the two warmest stages of refrigeration.

The coax electrical lead losses are based on the Coax configuration given in the design requirements. These losses are based on staging the electrical leads at the radiation shields. The lengths of the leads between stages one and two are doubled by looping the leads inside the thermal insulation in order to reduce thermal conduction. Results are reported in Table 1.

The net thermal radiation loss associated with each stage, including the radiation shields attached to stages one and two, was based on the use of 40 layers per inch of aluminized mylar insulation throughout the vacuum shell. Results are shown in Table 1.

System weights and volumes resulting from the interface study are given in Table 2. The input power requirement of 205 watts is dominated by cooldown time and not thermal loads or losses. The weights and volumes of Table 2 do not include the impact of magnetic shielding and vibration abatement.

TABLE 1

INTERFACE THERMAL LOADS

Stage	1	2	3	4
10 cm Diameter by 10 cm long				
Shield Length, cm	24.4	18.8	-	-
Shield Dia., cm	13.0	10.9	-	-
Radiation Loss, watts	0.047	0.054	0.002	0.007
4 cm Diameter by 15 cm long				
Shield Length, cm	29.4	23.8	-	-
Shield Dia., cm	7.0	4.9	-	-
Radiation Loss, watts	0.035	0.035	0.002	0.004
Coax Electrical Lead				
Loss, watts	0.046	0.056	-	0.012

TABLE 2

SYSTEM WEIGHT AND VOLUME*

ELECTRONICS VOLUME	SYSTEM WEIGHT	WEIGHT GOAL	SYSTEM VOLUME	VOLUME GOAL
10 cm Dia. by 10 cm LG	4970 g	4540 g	5950 cm ³	9800 cm ³
4 cm Dia. by 15 cm LG	4130 g	4540 g	3740 cm ³	9800 cm ³

*Does not include effects of magnetic shielding. Including the magnetic shields, the weight and volume for the 4 cm dia. x 15 cm LG electronics volume are:

Total system weight = 14700 grams
Total system volume = 14600 cm³

Thermodynamic Optimization

The object of the thermodynamic optimization was to improve the system efficiency by choosing a combination of thermodynamic parameters resulting in minimum input power. Parameters investigated were stage diameter, stage length, radial gap between the displacer and cylinder, minimum pressure, maximum pressure, speed, and stroke. The parameter effecting input power most sensitively was stage diameter.

Figure 1 shows illustrative results of the stage diameter study. Curve D_{22} shows the input power vs second stage capacity. Moving to the right represents an increase in the second stage diameter. This graph was used in conjunction with a graph of capacity vs. diameter to determine the second stage diameter at a desired capacity. The change in stage one net capacity corresponding to the change in input power caused by the stage two capacity change is shown as D_{21} . The first stage diameter would need to be adjusted to regain the capacity by using D_{11} which results in another change in input power. The effective coupling of the stages with diameter is therefore illustrated. Curves D_{23} and D_{24} show that changing the second stage diameter (and input power) has no effect on the capacity of stages three and four.

Figure 2 shows the results of the same type of study for stage length. The same general trends are present; however, the capacity isn't as sensitive to stage length as it is to stage diameter.

Figure 3 gives the results of the study applied to the radial gap between the displacer and the cylinder. Gap is less sensitive than either length or diameter.

Figure 4 shows the results of the optimization study for minimum pressure. Stage diameter was varied to maintain stage capacity as the minimum pressure was varied. The 61.5 psia used in the design is at the edge of the broad shallow minimum of the curve.

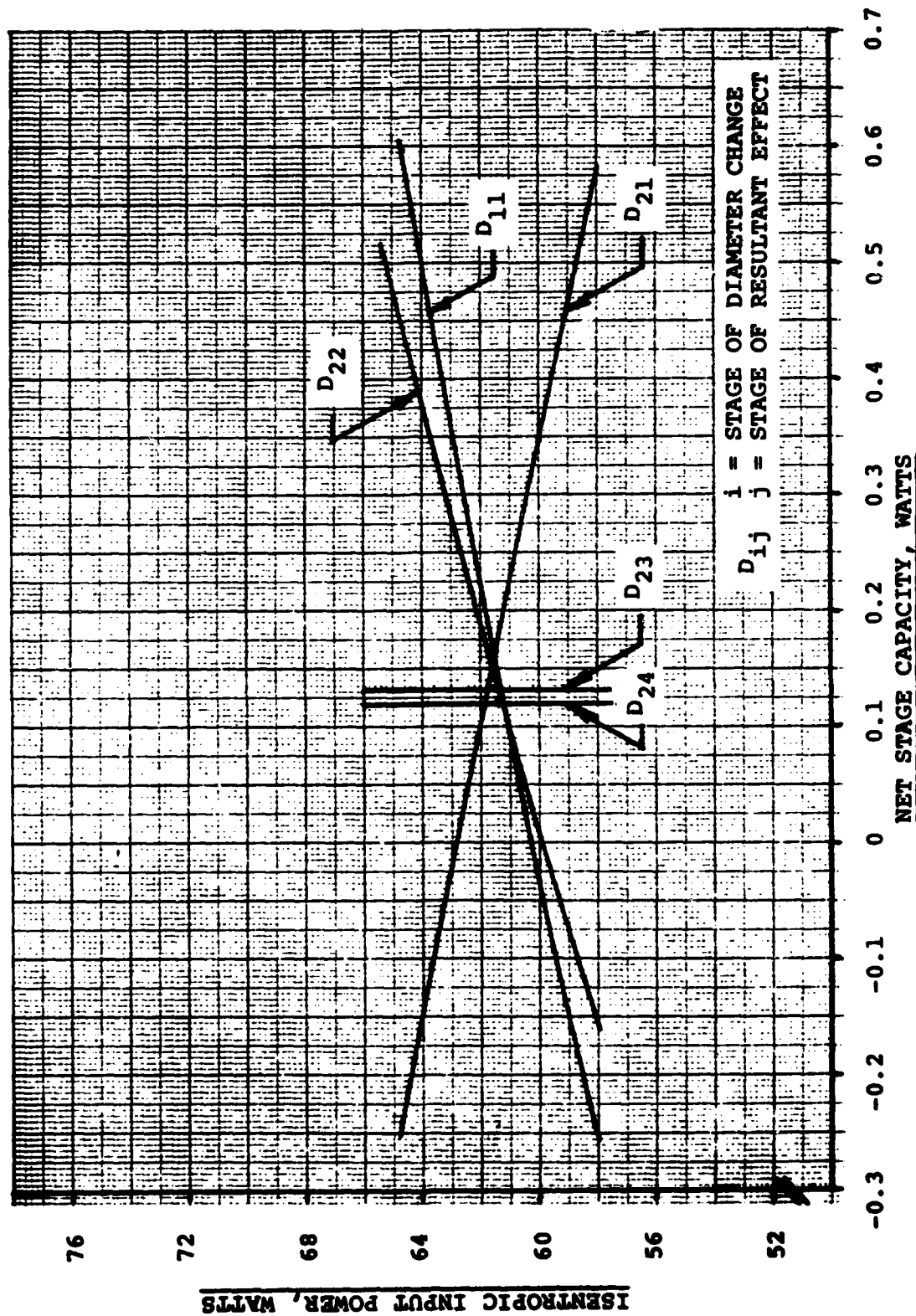
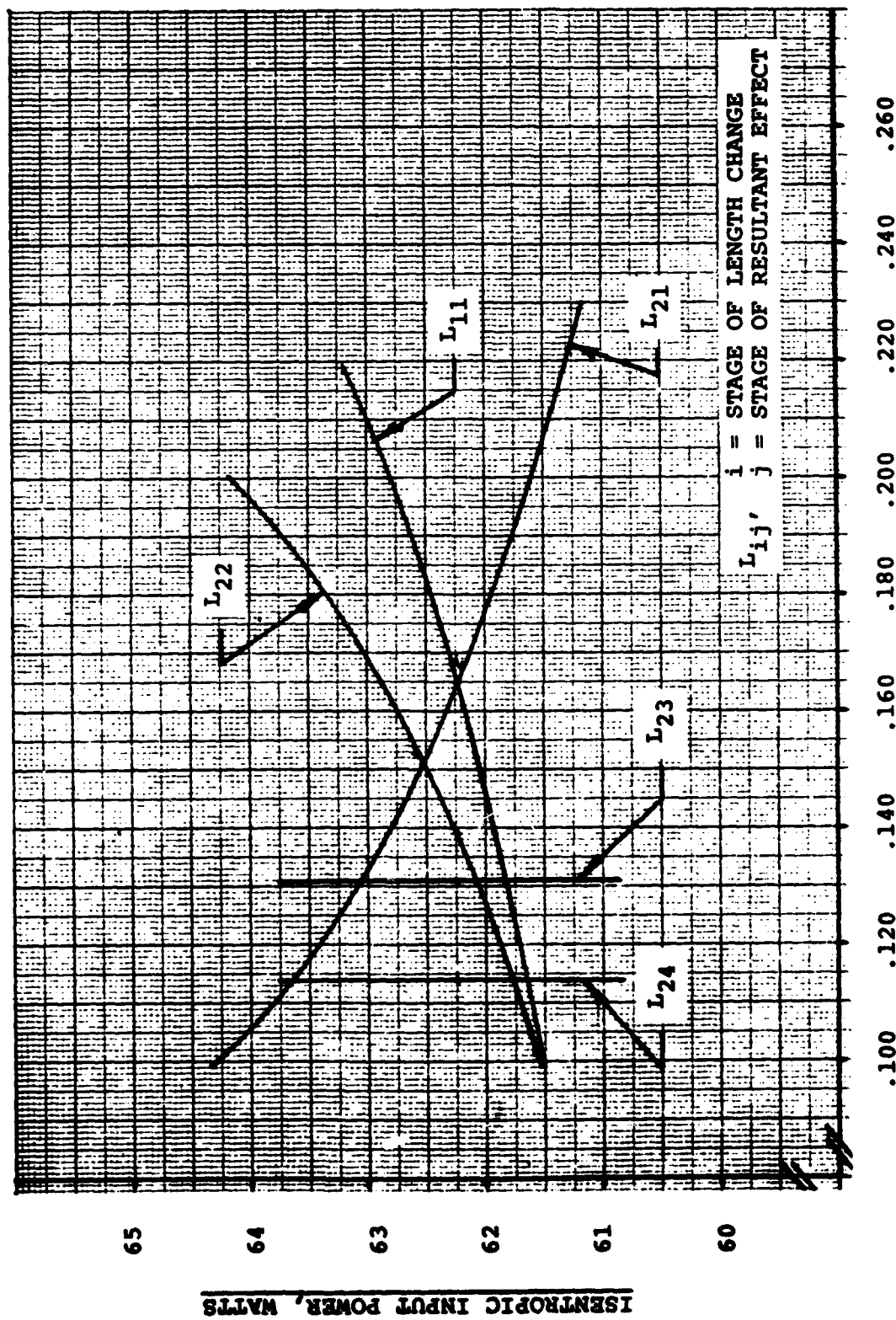


Figure 1: Small MACOR Concept, Diameter Study



NET STAGE CAPACITY, WATTS

Figure 2: Small MACOR Concept, Stage Length Parameter Study

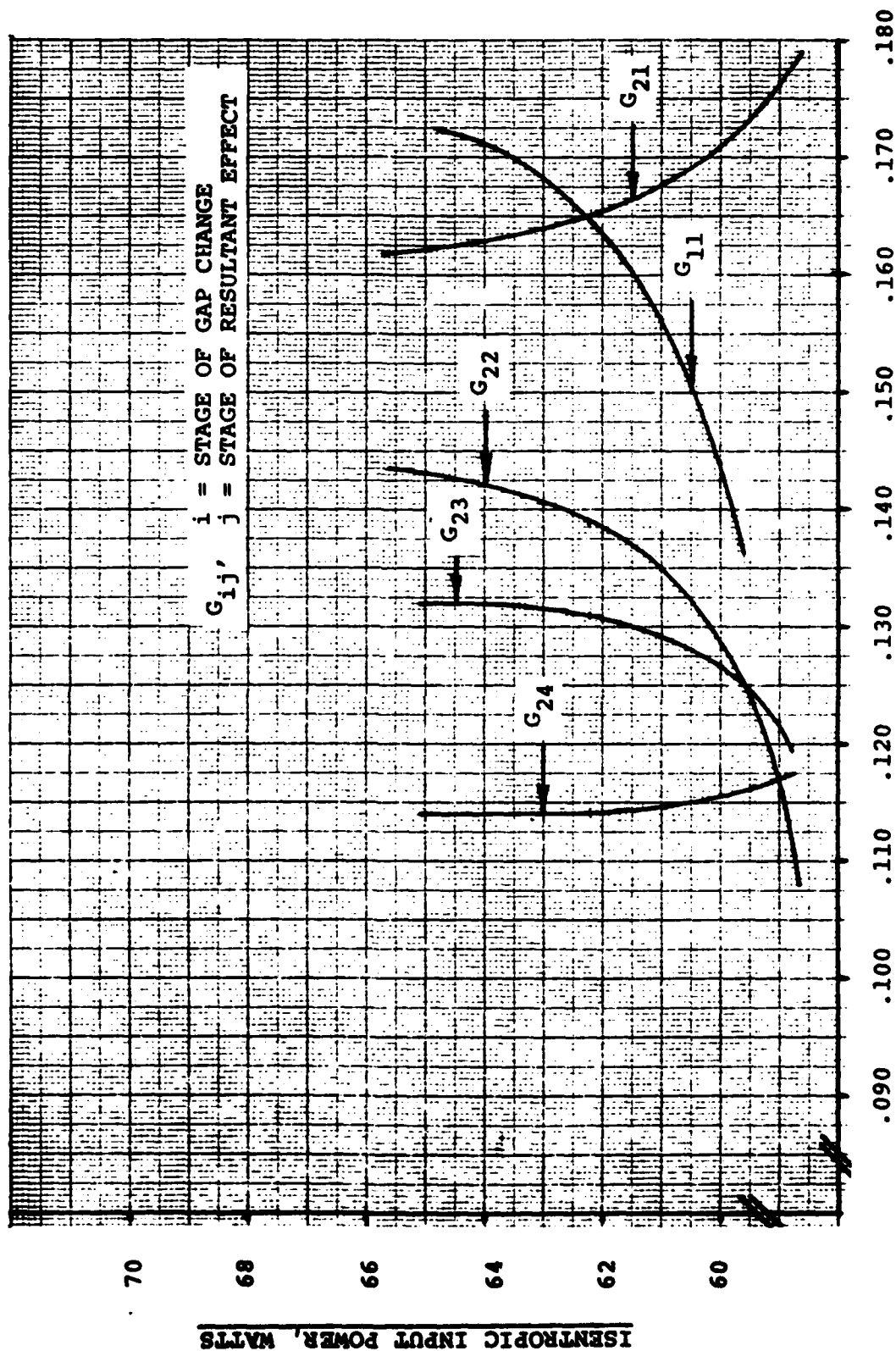
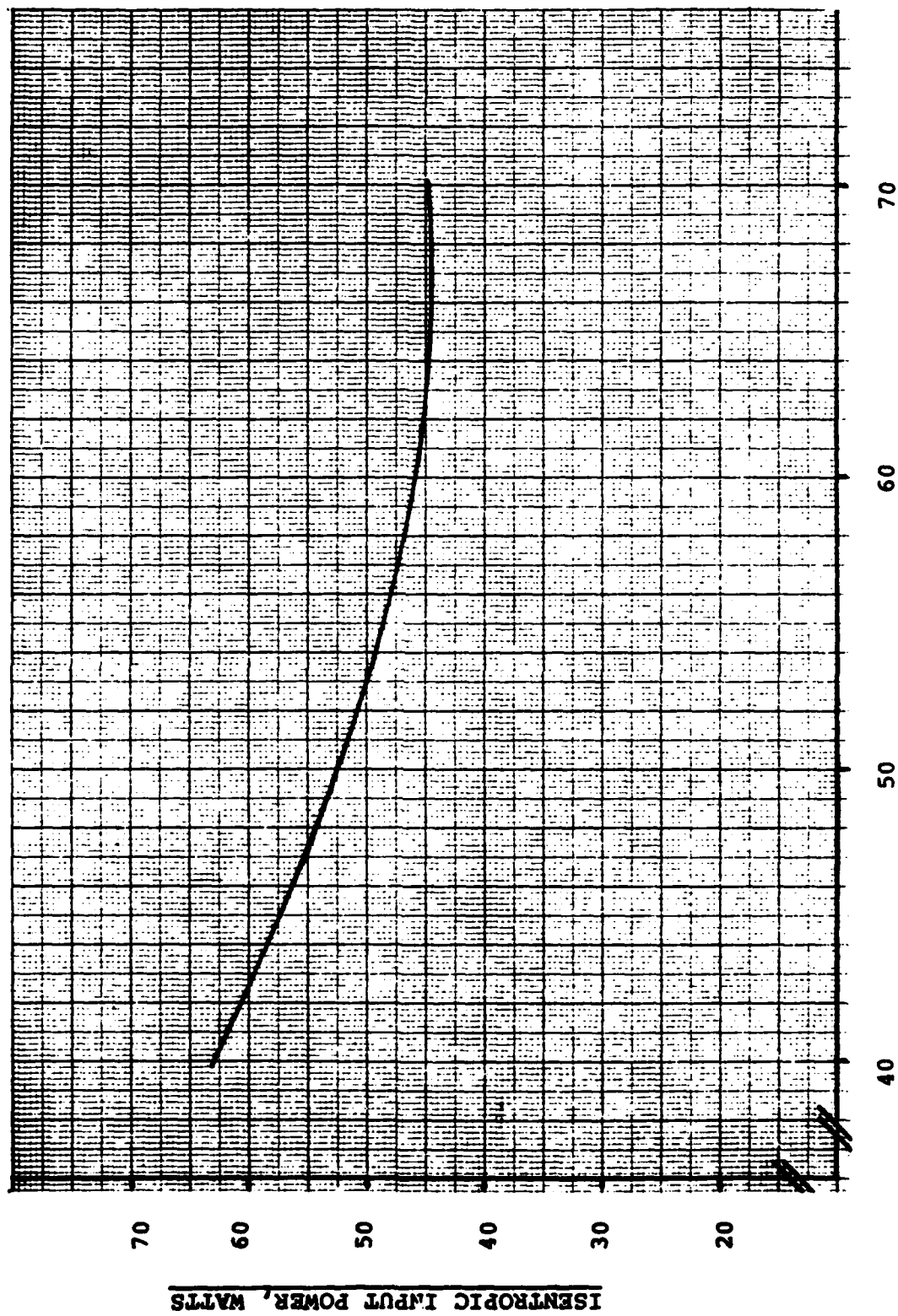


Figure 3: Small MACOR Concept, Gap Thickness Parameter Study



MINIMUM PRESSURE, PSIA

Figure 4: Small MACOR Study, Input Power Vs. Minimum Pressure For Constant Stage Capacity

Results for maximum pressure are shown in Figure 5. The 95.0 psia chosen for the design is represented by the weak minimum of input power.

No minimum was found for input power vs speed up to 2000 RPM. This speed was judged to be an upper limit for reliable operation.

Figure 6 shows the results of the study using stroke. A stroke of 0.1 inches was used in the design.

Thermodynamic Results

The results for the optimized cryocooler are given in Table 3. The cooler represented is the optimized result that achieves the program specifications and the required approximately 24 hour cooldown time. The 24 hour cooldown time increases the electrical input power from 140 watts previously reported to 205 watts.

Low Temperature Capacity

The estimated thermal capacity of Stage 4 of the preliminary design for temperatures below 10 K is shown in Figure 7. Since the specific heat of the displacer and cylinder walls that serve as the regenerators diminishes rapidly below 10 K, the ability to produce refrigeration also decreases. The result is that the net thermal capacity reaches zero at approximately 7.4 K. At the design no load temperature of 8 K, the estimated capacity is 60 milliwatts. The surplus capacities at 10 K and 8 K occur because cooldown time instead of steady state capacity drives the design.

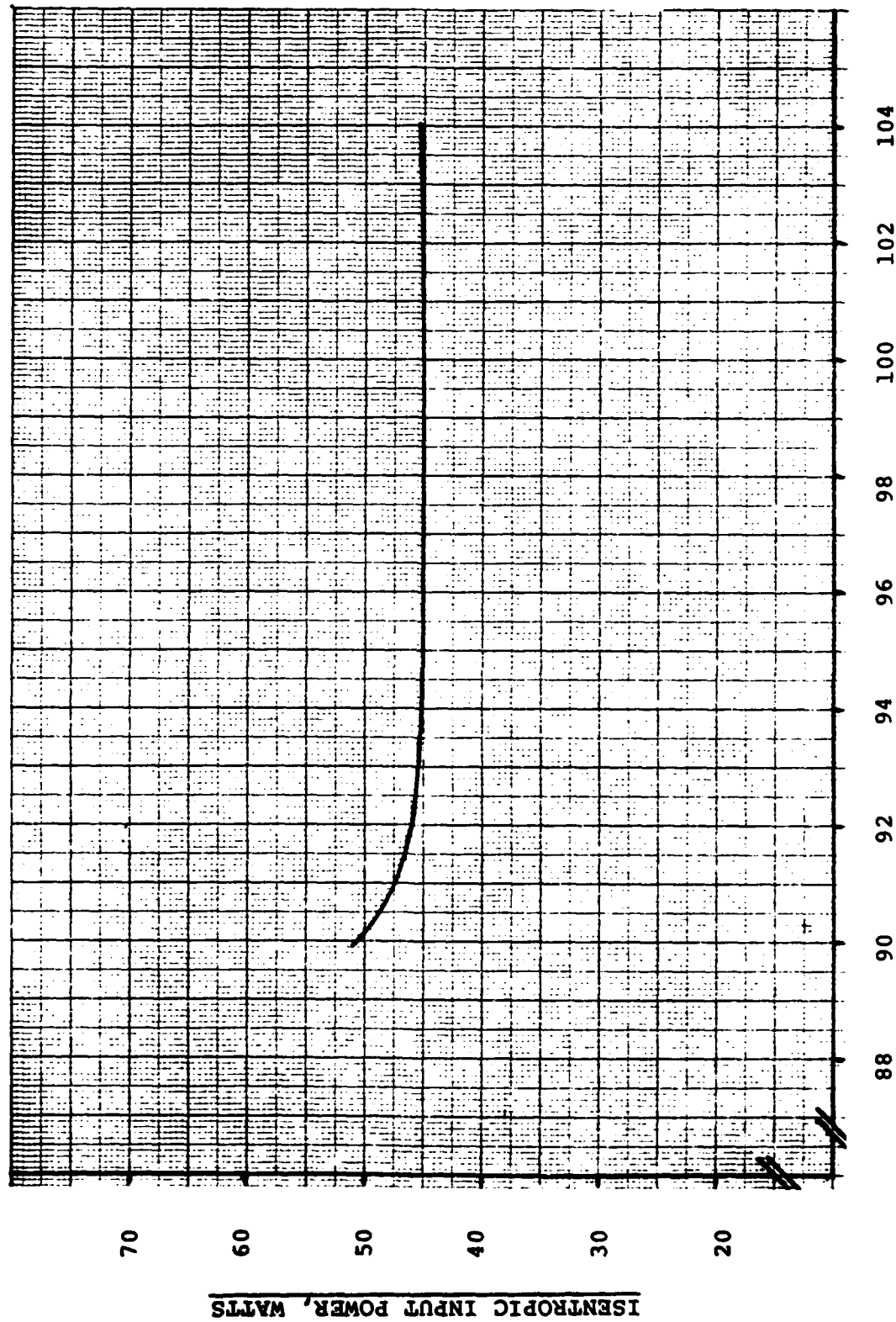
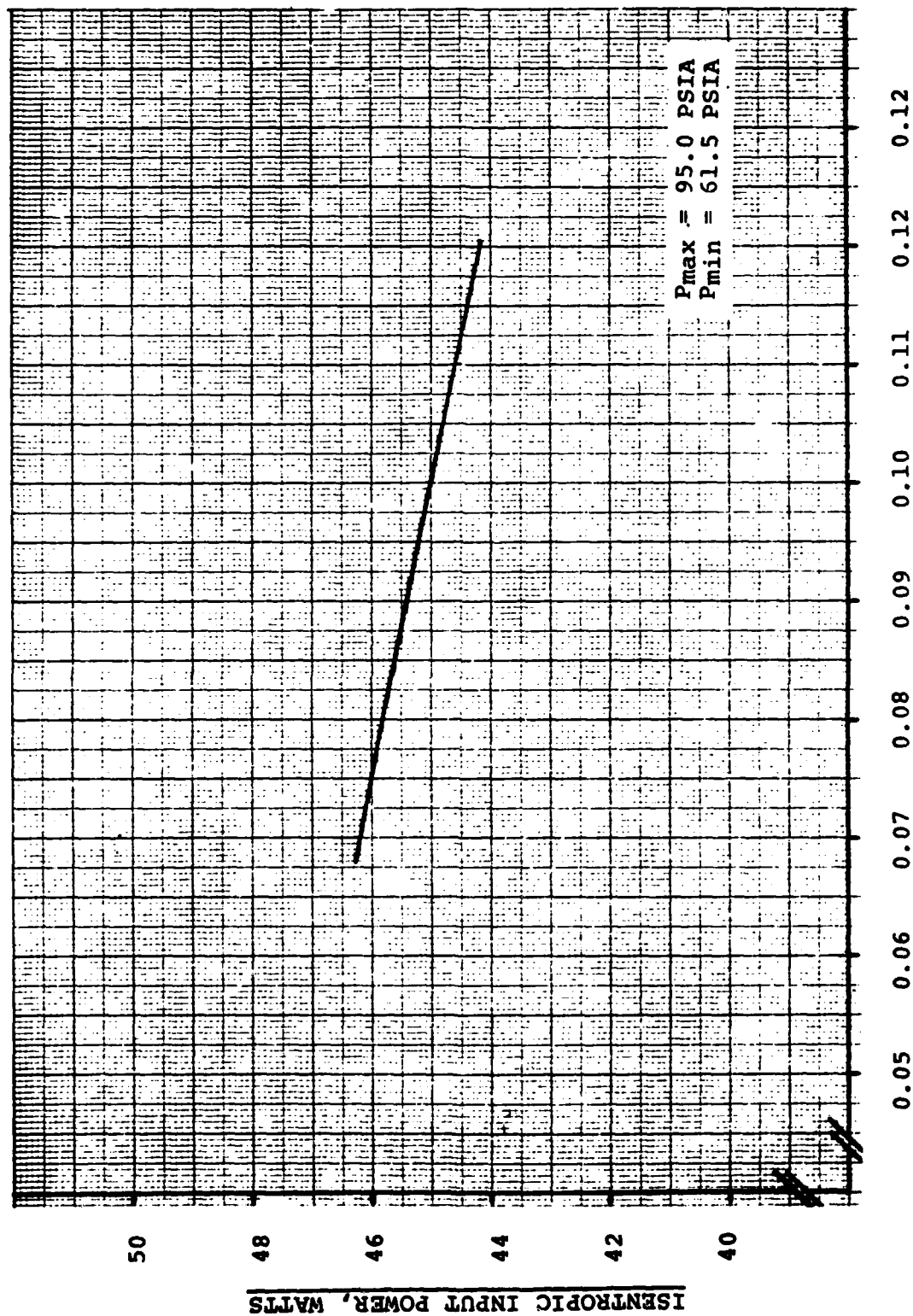


Figure 5: Small MACORTM Study, Input Power Vs. Maximum Pressure For Constant Stage Capacity



STROKE, INCHES

Figure 6: Small MACORTM Study, Input Power Vs. Stroke Length For Constant Stage Capacity

TABLE 3

PRELIMINARY DESIGN PARAMETERS

<u>STAGE</u>	<u>1</u>	<u>2</u>	<u>3</u>	<u>4</u>
CYLINDER DIA., CM	2.39	1.88	1.34	0.94
RADIAL GAP, CM	0.013	0.010	0.010	0.010
WALL THICKNESS, CM	0.160	0.160	0.160	0.160
REGEN LENGTH, CM.	5.08	5.08	5.08	2.54
MASS FLOW, g/s	0.240	0.202	0.164	0.114
NET CAPACITY, WATTS	0.144	0.142	0.024	0.115
TEMPERATURE, K	180	80	30	10

INPUT POWER = 205.0 watts

CYCLE RATE = 2000 RPM

STROKE = 0.25 cm

SYSTEM PRESSURES

MAX. = 6.46 atm (95.0 PSIA)

MIN. = 4.18 atm (61.5 PSIA)

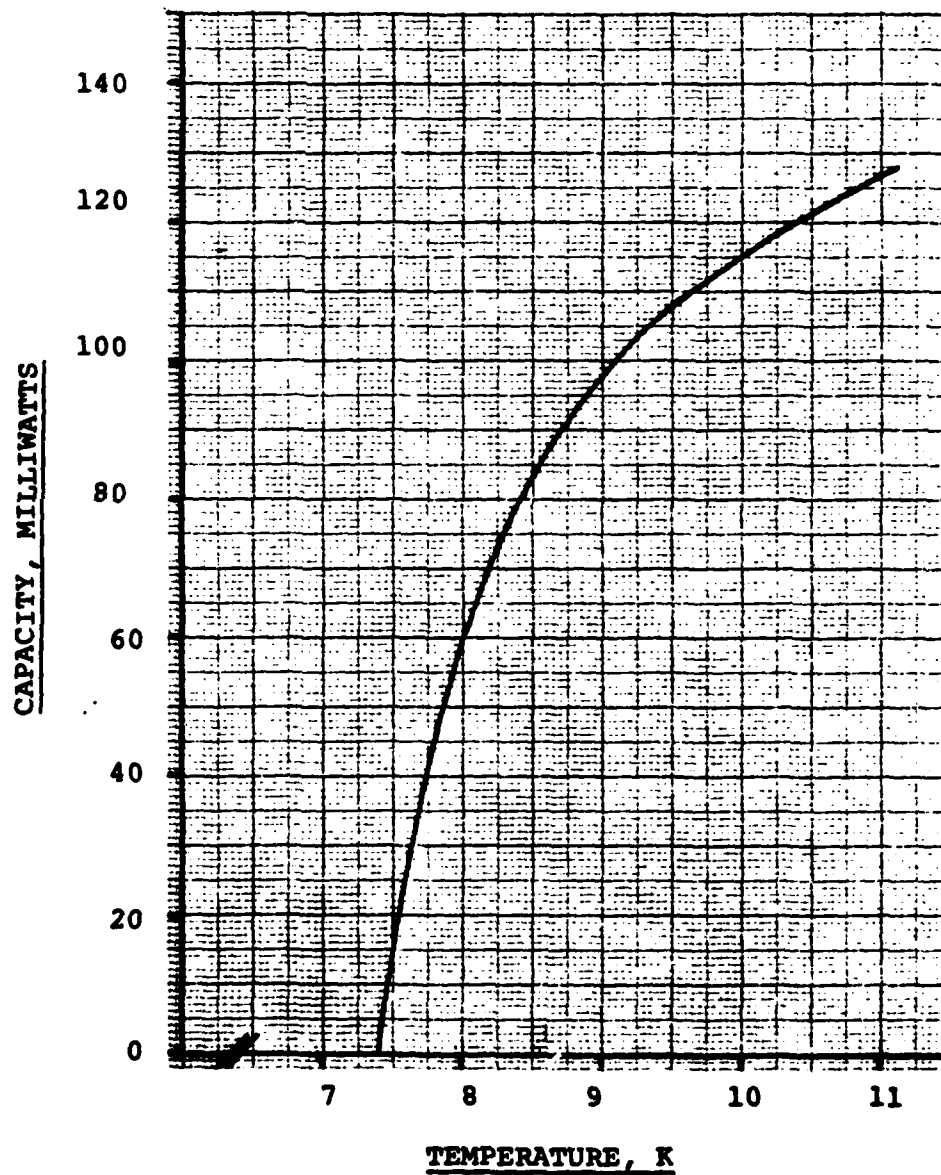


Figure 7: Preliminary Design Capacity Below 10K

Cooldown Time

The system was designed to cool the 300 grams of electronics from ambient temperature to operating temperature in approximately 24 hours. The cool-down curves for the four stages of the cryocooler operating in normal cool-down are shown in Figure 8.

Estimates were made of the cooldown time with 150 grams of electronics and with zero electronics mass. Approximately 19 hours are needed to cool 150 grams and approximately 8 hours are needed to cool only the cryocooler with no electronics mass.

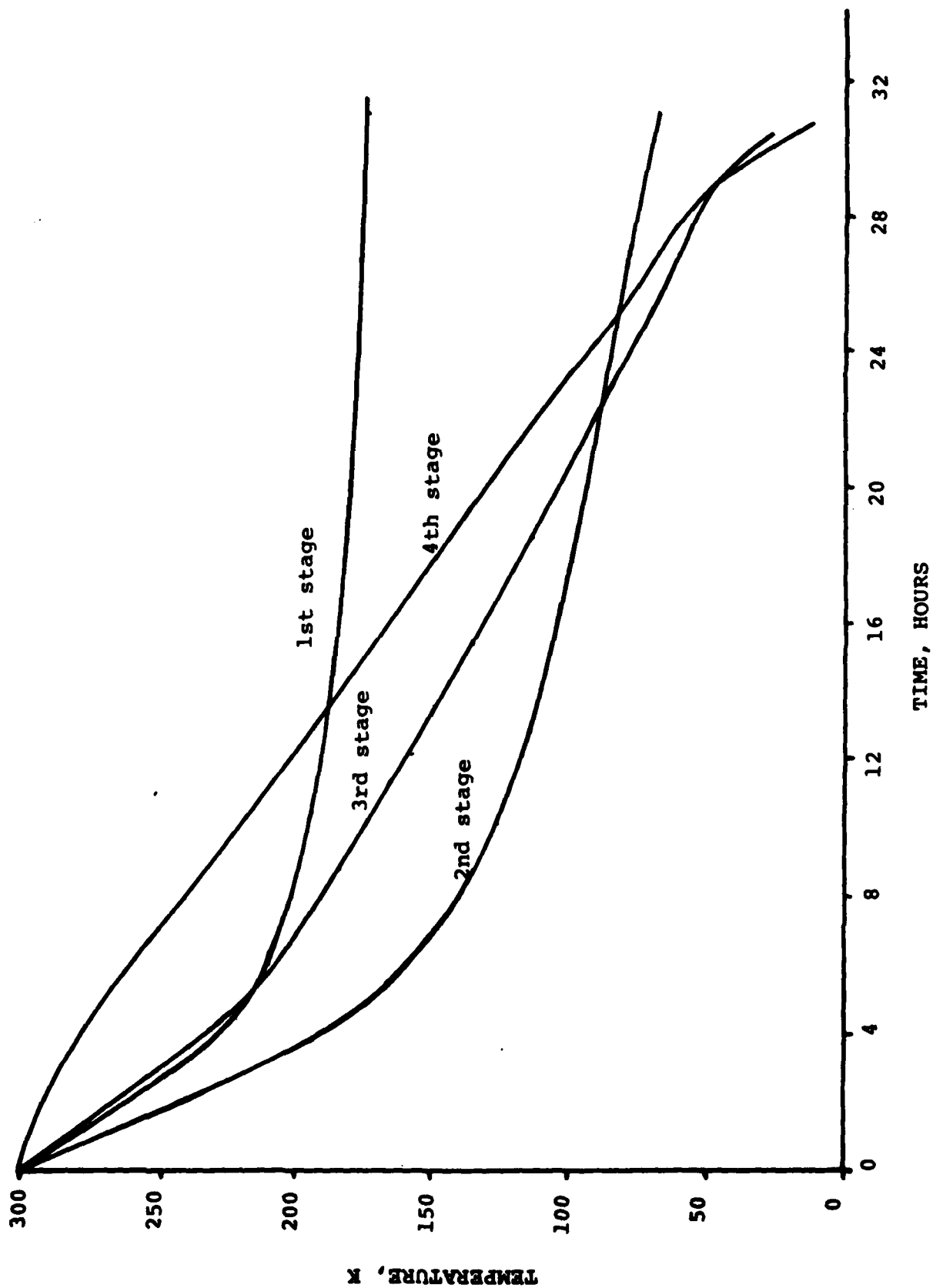


Figure 8: Preliminary Design, Cooldown Curves For Each Stage

IV. MECHANICAL DESIGN

General

The gap regenerator concept requires a high speed reciprocating displacer which is held concentric to a precision stepped coldfinger constructed of MACORTM machineable glass-ceramic. In order to insure a constant phase angle between displacer and compression pistons and to maintain a constant stroke, an integral Stirling cycle design was chosen over a split Stirling design with a remote compressor. The two disadvantages of the integral unit are:

- the electromagnetic fields of the drive motor are closer to the 10 K tip of the coldfinger,
- the compression pistons are a source of harmonic forces which can excite vibrations of the coldfinger tip.

Both problems can be solved by conventional electromagnetic shielding techniques along with inertia force balancing. The natural frequencies of various refrigerator components can be designed to be higher than the frequencies of interest to the refrigerator user.

A split system also has disadvantages including a higher power requirement, decreased reliability and more difficult cold end balancing. After consideration of the advantages and disadvantages of integral and split systems, the integral system approach was chosen.

The preliminary mechanical design is shown in Figure 9. The balanced compressor unit is surrounded by four layers of magnetic shielding with the outer shield also serving as the pressure vessel. Major design features are itemized below.

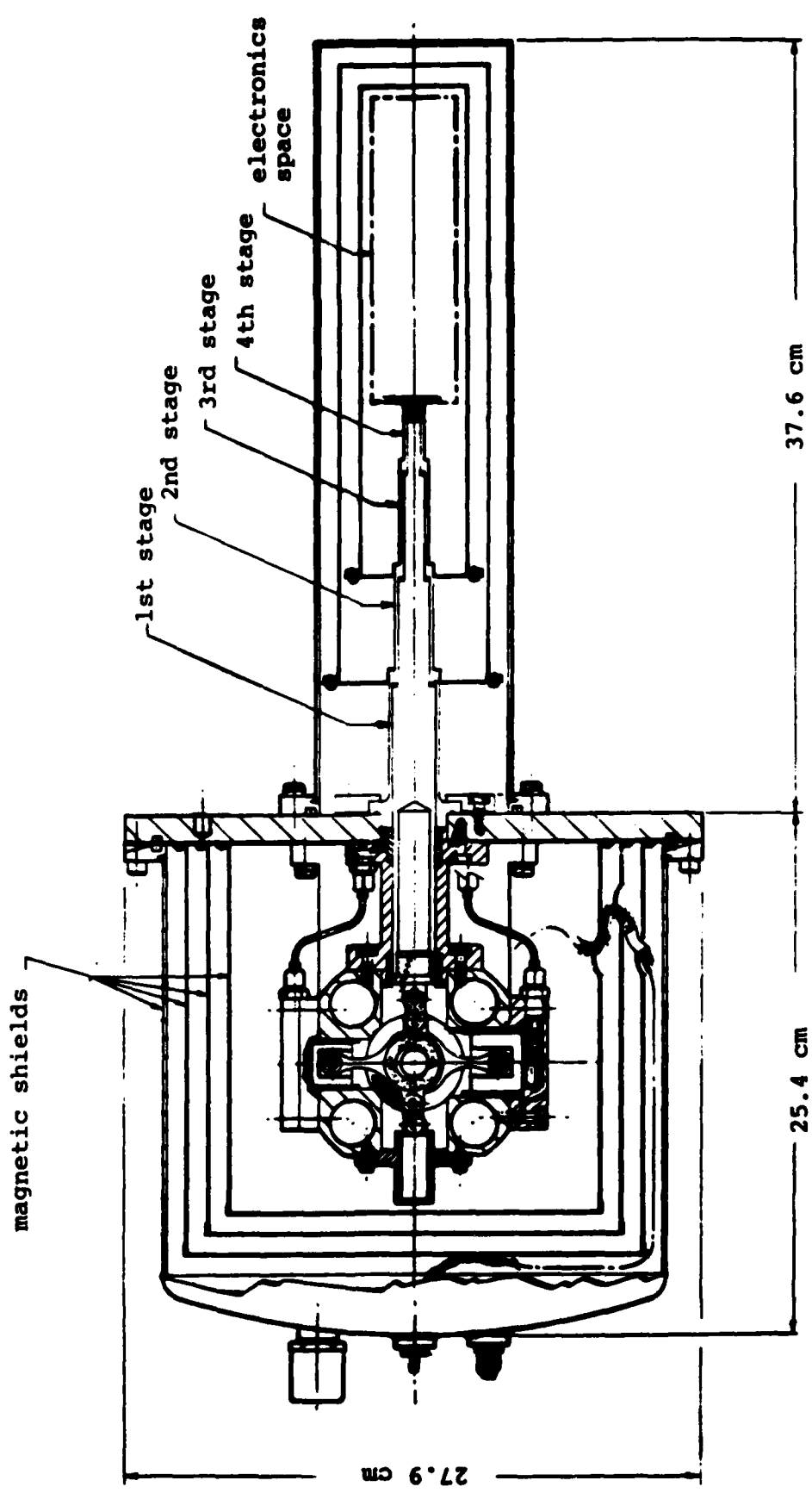


Figure 9: Preliminary Mechanical Design

Major Design Features and Tradeoffs

- A simple direct drive motor without gearing or auxiliary shafts and bearings.
- A dynamically force balanced piston-displacer system for low vibration signature.
- A rigid mounting plate to reduce rotational vibration (swaying) of the coldfinger and to provide heat sink capability for the motor and compressor heat rejection.
- A brushless DC drive-motor for high efficiency and a desirable torque vs. speed characteristic. Typical motor efficiency will exceed 70% at the load point.
- An open compressor design for reduced weight, reduced number of pressure seals, and ease of inspection and maintenance of the compressor (once the pressure housing and shield are removed).
- An array of four, high permeability, magnetic shields for proper attenuation of the magnetic field of 1500 gauss from the brushless DC motor. A magnetic support post together with a steel plate on top of the aluminum support plate complete the magnetic shield geometry. The fourth shield is also the hermetic container for the helium gas charge of about 75 psia.
- Rugged anti-friction roller bearings are used on each piston connecting rod along with ball bearings for the main shaft bearings. Low vapor pressure grease is used as a lubricant.
- Clearance seals for both the compression pistons and the displacer eliminate Teflon ring wear and potential debris contamination problems.

- A "die post" design for guiding the displacer insures that it will reciprocate and hold the required gap relative to the inside surfaces of the coldfinger tube. This feature will eliminate displacer/cylinder sliding contact that would generate unwanted heat sources at any of the four refrigeration stages.
- A displacer and coldfinger is constructed of MACORTM for low magnetic signature, low thermal conductivity and low thermal diffusivity at 10 K.

V. MACORTM MAGNETIC SUSCEPTIBILITY REDUCTION

A program was undertaken to lower the paramagnetic susceptibility of MACORTM machinable glass-ceramic through a reduction of the total Fe^{3+} and Mn^{2+} concentration, those ions being the main contributors to susceptibility through their unpaired electrons. The basic difficulty in this area is that, in nature, Fe and Mg are closely associated and it is difficult to find pure natural sources of magnesium, which is a constituent in MACORTM. Additionally, the machinable glass-ceramic contains fluorine. There are few sources of fluorine which are iron free.

The program consisted of using specially selected low iron raw materials to produce experimental machinable glass-ceramic samples, determine magnetic and thermal properties of the samples, and compare the results with the program requirements.

The details of the program description are given in Appendix A. The 118 DIV material, with 16 PPM of iron resulted in a significant reduction in susceptibility (Table 7). The results indicate a paramagnetic component reduction of about 27 times. Another significant result is the low susceptibility reported for standard MACORTM. This will allow standard MACORTM to be used in the design directly without the need for the special material.

Results shown in Tables 8, 9, 10, in Appendix A indicate that the thermal and mechanical properties of the developed low iron material are largely unchanged from standard MACORTM. Indications are that the specially selected raw materials do not change material properties except magnetic susceptibility.

Conclusions From Magnetic Susceptibility and Property Study

- Reduction of the paramagnetic susceptibility of standard MacorTM machinable glass-ceramic was achieved through a decrease in iron content. This decrease in susceptibility from 245×10^{-7} to $9.1 \times 10^{-7} \text{ cm}^3/\text{g}$ was achieved while essentially maintaining other physical properties at their nominal values.

- The low magnetic susceptibilities of standard MACORTM reported in Table 6 indicate that the standard material (500 PPM iron nominally) can be used directly in the preliminary design without producing unacceptable magnetic signature.
- The low iron 118 DIV material will serve as a back up or substitute for standard MACORTM in the event that the very low magnetic susceptibility is required for future applications.

VI. MACORTM HELIUM PERMEATION STUDY

Introduction

MacorTM, like all nonmetallics has a finite permeability to helium gas. Its permeability is less than boro-silicate glass which is commonly used in vacuum apparatus. Nevertheless, helium would diffuse through the walls of the MACORTM coldfinger to increase the absolute pressure in a permanent vacuum vessel enough to render the vacuum insulation useless. In order to use MACORTM effectively as a non-magnetic coldfinger material, its diffusion rate must be reduced several orders of magnitude by coating the outside surfaces with a metal.

Helium diffusion through MACORTM is analogous to heat transfer where the governing diffusion equation is:

$$Q = KA \frac{\Delta P}{\Delta X}$$

The diffusion constant K is quoted by Corning Glass Works to be 4.2×10^{-12} scc mm/sec cm²cm Hg at 143°C (416 K). For a cold finger tube of 72.9 square centimeters of surface area and an internal pressure of 5.1 atm, the helium diffusion rate is approximately $7.4 \times (10)^{-8}$ standard cubic centimeters per second.

The object of this study was:

- To verify that the quoted diffusion constant is reasonably accurate.
- To find and develop a thin metallic coating which could be evenly applied to the outside walls of the MACORTM coldfinger tube to eliminate diffusion.

According to Dushman (2) (page 570); "rare gases and polyatomic molecules do not diffuse noticeably through metals". The metal coating must be thin enough so as not to add excessive heat leak to the cryogenic regions of the refrigerator.

Results

A fixture was made to hold a MacorTM disk with a 6.45 square centimeter diffusion area at a thickness of 0.157 centimeters. A male port on the fixture fastened directly to the vacuum port of a mass spectrometer. The observed helium diffusion rate was measured to be 3.0×10^{-9} scc/sec with a 4.4 atm charge. The calculated diffusion rate shown in Table 4., was 5.7×10^{-9} scc/sec for the 6.4 square centimeter sample.

Discussion

The diffusion constant from the Corning brochure certainly gives a valid upper bound on the diffusion rate without adjusting the constant for room temperature from 143°C.

Our first attempt at a low diffusion metallic coating was a 0.2 mil (0.0002-inch) titanium coating, vacuum sputtered by the Hitman Company of Columbia, Maryland. Titanium has a low thermal conductivity and is non-magnetic. Unfortunately the diffusion rate of the titanium coated sample (5.4×10^{-9} scc/sec) was the same order of magnitude as the uncoated sample. Further discussion with Mr. Harold Barr at Hitman Company revealed that porosity in coating could explain the high leak rate. As a result of discussions with Hitman, the following procedure is recommended to produce a coating impervious to helium:

- a sputtered base coat of $5.08(10)^{-4}$ cm (2×10^{-4} inch) titanium,
- a second sputtered coat of $1.27(10)^{-3}$ cm (5×10^{-4} inch) silver/copper eutectic,
- Vacuum remelt at 800°C for 1 to 2 minutes to flow the eutectic.

The method offers promise in eliminating helium permeation, but it has not yet been verified experimentally. Further effort in this area is needed in order to be certain that the helium permeation can be prevented.

TABLE 4

HELIUM PERMEATION RATES

<u>P₁</u>	<u>P</u>	<u>Q (observed)</u>	<u>Q (calculated)</u>
3.4 atm	4.4 atm	3.0×10^{-9} scc/sec	5.7×10^{-9} scc/sec
5.1 atm	6.1 atm	4.6×10^{-9} scc/sec	7.9×10^{-9} scc/sec

VII. VIBRATION ANALYSIS WITH MAGNETIC SIGNATURE

Vibration of various modes causes magnetic interference of the electronic devices. Angular movement of the coldfinger causes movement of the electronics in the Earth's magnetic field. This movement results in stray magnetic signals at the electronics. Pressure stretching of the coldfinger due to the pressure wave associated with the Stirling cycle also produces movement and, consequently magnetic signature at the end of the coldfinger. Another signature is produced by the stroking of the displacer as the refrigeration cycle is accomplished. The expected vibrational characteristics and the resulting magnetic signals from these sources are treated in the following text.

Angular Movement

The angular movement is excited by the cycle torque due to the unbalanced angular acceleration of the piston rods in the cryocooler. The model for the analysis is shown in Figure 10. Results are:

Coldfinger natural frequency = 104.1 Hz
Compressor Package natural frequency = 312 Hz
Coldfinger deflection = $7.6 (10)^{-6}$ cm/gram

Angular motion at cold tip:

Frequency	0 to Peak angular amplitude
33 Hz (fundamental)	$3 (10)^{-10}$ radians
66 Hz (1st harmonic)	$3(10)^{-8}$ radians
99 Hz (2nd harmonic)	$3(10)^{-10}$ radians

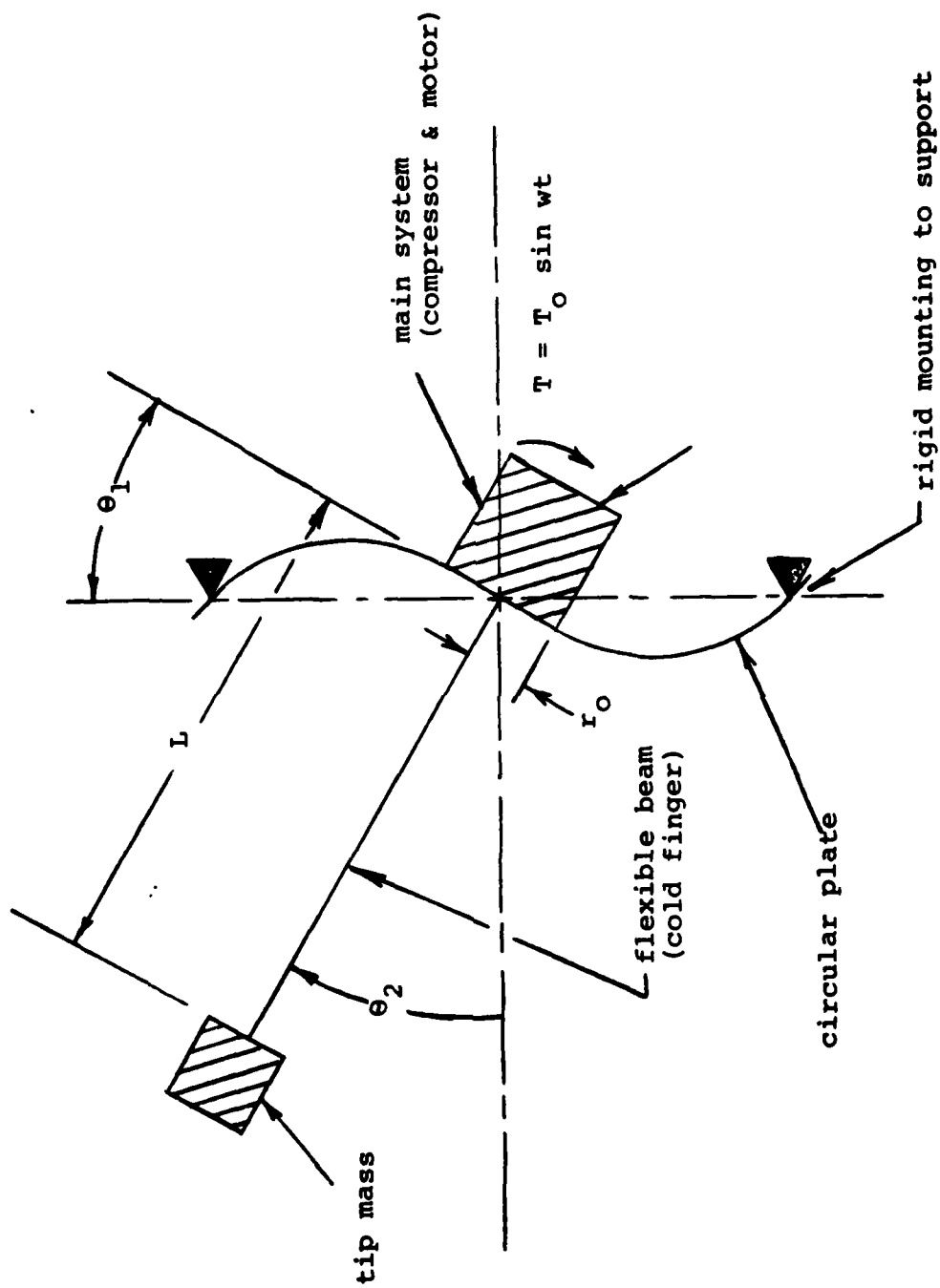


Figure 10: Model For Angular Vibration of Electronics

Magnetic signature arising from the angular vibration is given by the following discussion.

The field is given by:

$$H = H_0 \Delta\theta$$

where H_0 is the terrestrial field (0.5 gauss)
and $\Delta\theta$ is the angular movement.

Then the results are:

Frequency	0 to Peak angular amplitude
33 Hz (fundamental)	$1.5(10)^{-10}$ gauss
66 Hz (1st harmonic)	$1.5(10)^{-8}$ gauss
99 Hz (2nd harmonic)	$1.5(10)^{-10}$ gauss

Pressure Wave Stretching

The cycling pressure wave in the cold finger causes the cold finger to cyclically lengthen by $287 (10)^{-6}$ inches. The cold tip moves by this amount (Δx) axially through the gradient of the Earth's field ($G=0.01$ gauss /kilometer). The disturbance field amplitude is given by:

$$\Delta H = G \Delta x$$

$$\Delta H = 2.9(10)^{-11} \text{ gauss}$$

The frequency is 33 Hz corresponding to the cryocooler operating speed. This signature is several orders of magnitude less than the requirement.

Displacer Stroking

The movement of the displacer in carrying out the refrigeration cycle produces a magnetic disturbance at the electronics. For the case in which the terrestrial field is aligned with the axis of the displacer, the variation in the field on axis at a distance Z_0 from the mean position of the end of the displacer piston is given from Jackson (1) approximately by:

$$H = 1/2 H_0 \chi \frac{a^2}{(Z_0^2 + a^2)^{3/2}}$$

Where:

a = displacer stroke (0.254 cm)

a = displacer radius at 4th stage (0.300 cm)

χ = displacer magnetic susceptibility $(5.22(10)^{-6}$ at 10K for standard MACORTM)

H_0 = terrestrial field (0.5 gauss)

Z_0 = distance from the mean position of the end of the displacer (1.1 cm).

Then:

$$\Delta H = 2(10)^{-8} \text{ gauss at } 33.3 \text{ Hz}$$

Each of the magnetic disturbances given above is on the order of 10^{-8} gauss or less which are all within the 10^{-6} gauss specification.

VIII. DRIVE MOTOR MAGNETIC SIGNATURE ANALYSIS

Introduction

The proposed refrigerator will be driven by a pulsed DC motor whose rotor contains four permanent magnets. The objective of the present calculation is to estimate the magnetic noise at the end of the cold finger, due to the rotor magnets. Because the stator coils are pulsed, the fields which they generate will be at a higher frequency, and are not included in this calculation.

If the rotor is truly symmetric, the positions of the poles will repeat twice per revolution, and the fundamental frequency of the magnetic noise which it generates will be twice the rotor frequency, or 66.6 Hz. Asymmetry in the rotor can produce a signal at the rotor frequency, but with reasonable rotor manufacturing tolerances, this field is at least an order of magnitude smaller than the field of the rotor magnet.

The motor and drive system are mounted on an aluminum plate (thickness 0.5") and is surrounded by several cylindrical magnetic shields as shown in Figure 9. The displacer piston passes through a circular hole in the plate, which is not on the axis of the shielding cans. The magnetic noise at the end of the cold finger is due to leakage through the shields (including the plate) and through the displacer hole in the mounting plate.

Since there are no applied currents, the magnetic field is derivable from a scalar potential, and the calculation can use analogies from electrostatic potential theory. The geometry of the internal structures (some of which include magnetic materials) is however quite complex. A precise calculation of the leakage fields would be complicated, certainly requiring numerical integration of Poisson's equation. Fortunately, we are only interested in an estimate of the magnetic noise, so that an approximate calculation will suffice.

The steps in the calculation are as follows:

The inner magnetic shield is initially assumed to have infinite permeability. This means that the field at the inner surface of the can is normal to the surface: this is a good approximation for high permeability shielding materials. The inner surface of the shield is then a magnetostatic equipotential. The fields inside the can are then calculated from potential theory, ignoring magnetic materials in the drive system (other than the rotor poles).

Approximate shielding factors for the cans are then calculated, using a much simpler magnetic configuration but realistic permeabilities. This calculation is extended to the case of multiple shielding cans, to allow estimation of their effects and of the spacing between them. The fields outside the can are obtained by dividing the internal field (calculated in step 1) by the can shielding factor and extrapolated to give an estimate of the leakage field through the shields, at the end of the coldfinger.

The field in the displacer hole will be smaller than that calculated in step 1 at this location, especially because the hole is surrounded by a ferromagnetic collar. The field at the hole location is nevertheless extrapolated to give an upper bound to the leakage field from this source at the end of the cold finger.

The development of the appropriate equations and the details of the analysis are given in Appendix B. The results are given briefly in the following text.

The rotor contains 8 poles, one at each end of the four rotor magnets, of pole strength $P=430$ in Gaussian units. Coordinates of the 8 poles are given in Table 11 in Appendix B. The poles were used to develop the field inside the inner shielding can. Figure 11 shows the field inside the can at the base plate along the line parallel to the motor axis from $-R$ to R (shield radius). The maximum field caused by the rotor is 6.8 gauss and the field at the location of the displacer hole is 5.9 gauss. The peak is displaced slightly from the centerline because of the asymmetric positions of the rotor poles.

The shielding factors from 1 through 4 shields are shown in Figure 13. The figure shows that for interior fields of order 5 gauss, four shields ($\mu=10^5$) should be adequate to achieve the required 10^6 shielding factor.

Leakage through the displacer hole is expected to be approximately 2×10^{-7} gauss which is within the program specifications. This was based on the 5.9 gauss field at the displacer hole, and the cubic decay law of the field for points far from the source.

Conclusions Based on Magnetic Signature Analysis

Magnetic field leakage through the displacer hole is not expected to be a problem. Confidence in this result would be increased if the high permeability collar around the displacer hole were extended for several centimeters below the baseplate. Alternatively, use of a high permeability plug in the upper end of the displacer piston would reduce the leakage field to negligible values. The motion of such a plug will introduce some distortion of the Earth's field, and hence a magnetic signature at the displacer frequency. However, the collar and the magnetic shields will reduce the Earth's field at the plug location to a value below 1 milli-gauss: a preliminary estimate suggests that the signature induced by the plug at the coldfinger would be well below 1 microgauss.

Leakage through the cylindrical cans should not be a problem if 4 cans are used and if the shield permeability approaches 10^5 . Leakage through the baseplate is, however, more serious. It appears that at least 3 and possibly 4 shields, depending on permeability, will be needed over the baseplate, separated by about 1 cm. It is not necessary that the circumference of the baseplate be shielded, since the distance effect will reduce leakage through the circumference to acceptable values. Provision should be made for at least one and preferably two additional baseplate shields, internal or external.

CONCLUSIONS

The Phase IIA program has yielded several conclusions which are listed as follows:

- The preliminary design satisfies the specifications for thermal capacity, input power, temperature stability, zero load temperature, and approximate cooldown time.
- The weight and volume goals are exceeded primarily because of the shield system needed to satisfy the magnetic signature requirement.
- A cryocooler coldfinger constructed of standard MACORTM will satisfy the magnetic signature specification.
- The MACORTM study resulted in a significant reduction in the paramagnetic susceptibility while maintaining other physical properties at their nominal values. This reduction can be considered a margin of safety that could be used in future designs requiring even lower magnetic signature.
- The magnetic signature caused by the drive motor at the electronics satisfies the 10^{-6} Gauss specification.
- Field leakage via the displacer hole is not expected to be a problem.
- Field leakage through 4 shields should not be a problem if shield permeability approaches 10^5 and if 4 shields are also used on the base plate.

APPENDIX A

MACORTM MAGNETIC SUSCEPTIBILITY AND PROPERTY STUDY

The program was performed by Corning Glass Works under a subcontract to CTI-CRYOGENICS. The purpose was to develop a lower magnetic susceptibility machinable glass-ceramic similar to MACORTM. Other thermal and mechanical properties were to be kept as constant as possible to standard MACORTM. The approach was to use low iron raw materials, specially selected, to produce the machinable glass-ceramic. The method and results are described in the following sections.

Composition

• Sample Preparation

Special low-iron raw materials were weighed in 1000 gram batches and ball milled using acid-washed mills. The batches were melted at 1450°C in new platinum crucibles and poured into clean graphite molds of 15.2 x 15.2 x 1.9 cm size. Pilot heat treatments used to convert the glass to a machineable glass-ceramic showed that a schedule of 950°C over 4 hours produced a medium to coarse grained material. This grain size was deemed to be slightly large, so that subsequent heat treatments were lowered to 930°C over four hours. The variation in heat treatment can be used to tailor the strength and machinability into acceptable ranges for this product. In addition, a Differential Thermal Analysis curve was run on the unceramed glass to verify its crystallization behavior.

Four lots of low-iron machinable glass-ceramic, herein called experimental composition 118 DIV were prepared. These lots are identified both by melt and sample numbers. The melt number identified the melting unit used and date of preparation, while the sample number refers to the individual crucible in a set of melts.

- **Chemical Analysis**

Glasses from each melt were sampled and analyzed for Fe, Ni, Mn and Co using a Perkin-Elmer 403 spectrometer with a graphite tube furnace excitation source. Additionally, analysis were made of the K_2O , B_2O_3 and F contents for these melts to verify the batching and melting procedures. The results of these analysis are given in Table 5. The variability in iron level is difficult to assess at this time. Although everyone has been cautioned on the handling of the batches and glasses, it is relatively easy to pick up minor contamination which can greatly effect the number recorded.

Properties

- **Magnetic Susceptibility**

Measurements of magnetic susceptibility were performed by Dr. F. Fickett at the National Bureau of Standards Laboratory at Boulder, Colorado. Samples of 3/16-inch OD x 3/4-inch length were supplied of both the experimental composition 118 DIV and standard MACORTM glass-ceramic. The instrument used was a superconducting magnetometer. Table 6 gives the results obtained for the total susceptibility of both materials at room temperature (293 K) and 4.0 K.

Since the total susceptibility is composed of the diamagnetic susceptibility and the paramagnetic susceptibility divided by T K, we can use the data obtained at the different temperatures to solve for the independent values of diamagnetic and paramagnetic susceptibilities.

For the standard material:

$$\begin{aligned} -2.99 \times 10^{-7} &= \mu_o + \frac{\mu'}{293} \\ +57.5 \times 10^{-7} &= \mu_o + \frac{\mu'}{4} \end{aligned}$$

$$\begin{aligned} -60.5 \times 10^{-7} &= \mu' \left(\frac{1}{293} - \frac{1}{4} \right) \\ \mu' &= 245 \times 10^{-7} \end{aligned}$$

For the experimental material:

$$\begin{aligned} -3.82 \times 10^{-7} &= \mu_o + \frac{\mu'}{293} \\ -1.58 \times 10^{-7} &= \mu_o + \frac{\mu'}{4} \\ -2.24 \times 10^{-7} &= \mu' \left(\frac{1}{293} - \frac{1}{4} \right) \\ \mu' &= 9.08 \times 10^{-7} \end{aligned}$$

Solving for μ_o , for the standard material:

$$\begin{aligned} -2.99 \times 10^{-7} &= \mu_o + 0.84 \times 10^{-7} \quad (\text{at } 293 \text{ K}) \\ +57.5 \times 10^{-7} &= \mu_o + 61.3 \times 10^{-7} \quad (\text{at } 4 \text{ K}) \end{aligned}$$

$$\begin{aligned} 54.5 \times 10^{-7} &= 2 \mu_o + 62.1 \times 10^{-7} \\ \mu_o &= -3.80 \times 10^{-7} \end{aligned}$$

Solving for μ_o , for the experimental material:

$$\begin{aligned} -3.82 \times 10^{-7} &= \mu_o + .03 \times 10^{-7} \quad (\text{at } 293 \text{ K}) \\ -1.58 \times 10^{-7} &= \mu_o + 2.28 \times 10^{-7} \quad (\text{at } 4 \text{ K}) \end{aligned}$$

$$\begin{aligned} -5.40 \times 10^{-7} &= 2 \mu_o + 2.31 \times 10^{-7} \\ \mu_o &= -3.86 \times 10^{-7} \end{aligned}$$

Specific heat was measured from -120 to 600°C using the Dupont 990 thermoanalyzer with the Differential Scanning Calorimeter cell. The data are tabulated at even temperatures in Table 10. A comparison of the specific heat data was made. These results were listed in Table 10. In general the agreement between the two materials was $\pm 2\%$, which is within the accuracy of the measurements.

- Thermal Conductivity

Measurement of thermal conductivity is made using a thermal comparator method which employs known standards to bracket the experimental material. The value obtained for the experimental composition 118 DIV at room temperature is 0.0039 ± 0.0003 cal-cm/cm²-sec-°C ($1.63 \text{ Wm}^{-1} \text{ }^{\circ}\text{K}^{-1}$). This value agrees well with the standard MACORTM glass-ceramic of 0.0037 cal-cm/cm²-sec-°C ($1.55 \text{ Wm}^{-1} \text{ }^{\circ}\text{K}^{-1}$).

- Strength

The conventional method of strength evaluation for ceramic materials utilizes a flexible bend test, providing a modulus of rupture or M.O.R. value, usually given in units of pounds per square inch (psi). Samples were ground to dimensions of $4 \times 3/8 \times 1/4$ -inch and the edges were slightly beveled. The samples were finished with a fine-grind surface (20 μ inch) and were then abraided by the ASTM standard procedure C-158.

The samples were loaded in four point flexure using a support span of 3.5 inches and a load span of 0.75 inch. The cross-head speed was 0.06 inches/ min. The nominal value of M.O.R. for standard material is 15,000 psi with a minimum specification of 13,500 psi. The values recorded for two lots of experimental material are given in Table 8. It should be realized that the lack of homogeneity and resulting variability in M.O.R. of small unstirred 1000 gram melts is a common problem.

- Machinability

A standard Corning Glass Works test for machinability utilizes a conventional light duty mechanical hacksaw. A counter-balance system is used to provide a blade pressure of about 6 lbs. Samples 1/2 x 1 x 6 inches are clamped in the vice so that the blade draws across the 1/2-inch dimension. A series of 5 cuts are taken along the length of the sample using 20 strokes per cut. The average depth of cut is taken as a relative measure of the ease of cutting and quoted as a "machinability index" as follows:

$$M.I. = \frac{S}{1/2 W (T_1 + T_2) 10} = \frac{S}{10A}$$

where S is the number of strokes, W the width of the samples, and T_1 and T_2 are the depths at each end of the cut. Two measurements of depth are required since the cut is made at a slight angle. A new Marvel 12 inch, 14 tooth high-speed blade (No. 1214N) is used for each sample. To correct for any fluctuations, a sample of cold rolled steel 1018 is run with the material of interest and the result for the steel arbitrarily scaled to a value of 111.

A nominal value of M.I. for the standard material is 25 with a range of acceptability from 13 to 70. The measured value for the experimental material, 118 DIV melt M-10-5319 sample 1, was 13.4 which is at the low (easy to machine) end of the range.

- Thermal Expansion

A comparison of the thermal expansion coefficients of the experimental and standard materials is given in Table 9. The small variances noted are within the normal range of expansion coefficients for these materials.

TABLE 5

CHEMICAL ANALYSIS OF EXPERIMENTAL COMPOSITION A

<u>Component</u>	<u>Melt</u> M-10-5319 <u>Sample 1</u>	<u>Melt</u> M-1-9629 <u>Sample 1</u>	<u>Melt</u> M-1-9629 <u>Sample 2</u>	<u>Melt</u> M-1-9629 <u>Sample 3</u>	<u>Standard</u> MACOR CU-14-76
XK ₂ O	9.20	12.7	10.2	10.1	12.0
XB ₂ O ₃	8.34	8.36	8.38	8.28	8.70
XF	6.44	5.62	5.56	5.54	6.68
ppm Fe	16	18	25	25	6×10^2
ppm Ni	<10	N/A	<10	<10	N/A
ppm Mn	< 2	< 1	< 1	< 1	30
ppm Co	<10	N/A*	<10	<10	N/A*

* if visible below detection limit of <10 ppm

TABLE 6

MAGNETIC SUSCEPTIBILITY DATA

<u>Material</u>	<u>Temperature (°K)</u>	<u>Mass (g)</u>	<u>Susceptibility (cm³/g)</u>
Standard S1-1	293	.785	-3.01 X 10 ⁻⁷
Standard S1-2	293	.785	-2.98 X 10 ⁻⁷
Experimental E1-1	293	.773	-3.76 X 10 ⁻⁷
Experimental E1-2	293	.775	-3.89 X 10 ⁻⁷
Standard S1-1	4.0	.785	+5.80 X 10 ⁻⁶
Standard S1-2	4.0	.785	+5.70 X 10 ⁻⁶
Experimental E1-1	4.0	.773	-1.57 X 10 ⁻⁷
Experimental E1-2	4.0	.775	-1.59 X 10 ⁻⁷

Composition 118 DIV Melt M-10-5319 Sample 1.

TABLE 7
**CALCULATED VALUES OF DIAMAGNETIC
 AND
 PARAMAGNETIC SUSCEPTIBILITIES (cm^3/g)**

	<u>Standard Material Code 9658</u>	<u>Experimental Material 118 DIV 15-10-5319</u>
Diamagnetic Susceptibility	-3.80×10^{-7}	-3.86×10^{-7}
Paramagnetic Susceptibility	245×10^{-7}	9.08×10^{-7}

TABLE 8**STRENGTH MEASUREMENTS ON EXPERIMENTAL MATERIALS****Composition 118 DIV Melt M-10-5319 Sample 1**

<u>Bar No.</u>	<u>MOR (psi)</u>
1	13,600
2	11,800
3	13,700
4	14,100
5	12,700
6	13,900
Average	13,300
% Deviation	6.6

Composition 118 DIV Melt M-1-9629 Sample 3

<u>Bar No.</u>	<u>MOR (psi)</u>
1	16,700
2	18,700
3	16,400
4	17,300
5	17,600
6	17,300
7	16,700
8	16,100
Average	17,100
% Deviation	4.9

TABLE 9
THERMAL EXPANSION COEFFICIENTS

	<u>Standard Material Code 9658</u>	<u>Experimental Material 118 DIV M-10-5319</u>
RT to 200°C	$89 \times 10^{-7}/^{\circ}\text{C}$	$89 \times 10^{-7}/^{\circ}\text{C}$
RT to 400°C	$94 \times 10^{-7}/^{\circ}\text{C}$	$89 \times 10^{-7}/^{\circ}\text{C}$
RT to 550°C	$104 \times 10^{-7}/^{\circ}\text{C}$	$100 \times 10^{-7}/^{\circ}\text{C}$

TABLE 10
SPECIFIC HEAT OF MACOR

<u>Temperature</u> <u>°C</u>	<u>Specific Heat, cal/cm.°C</u>		<u>%</u> <u>Difference</u>
	<u>119-SCR</u>	<u>118-DIV</u>	
-120	0.118	-	-
-100	0.133	0.131	1.5
- 80	0.145	0.143	1.4
- 60	0.157	0.156	0.6
- 40	0.166	0.164	1.2
- 20	0.176	0.174	1.1
0	0.188	0.186	1.1
20	0.194	0.193	0.5
40	0.201	0.200	0.5
60	0.208	0.206	1.0
80	0.213	0.213	0.0
100	0.221	0.218	1.4
150	0.235	0.231	1.7
200	0.247	0.244	1.2
250	0.258	0.254	1.6
300	0.264	0.262	0.8
350	0.270	0.269	0.4
400	0.276	0.278	0.7
450	0.285	0.294	3.1
500	0.304	0.314	3.2
550	0.306	0.315	2.9
600	0.309	0.324	4.6

APPENDIX B

MAGNETIC SIGNATURE DEVELOPMENT

This appendix contains the details of the development of the equations giving the rotor pole strength and coordinates, shield factors, and displacer hole leakage field.

Rotor Poles

The rotor magnets are specified as having a surface field strength, at the ends, of 1500 gauss. For use in the calculation, this figure must be converted into an equivalent pole strength. For this purpose, the magnets are taken as cylinders of length b and radius a ; the actual cross-section is not circular, but this is not expected to have a major effect.

If the magnet has a uniform axial magnetization \underline{M} (magnetic moment per unit volume) and if the pole strength is p , the magnetic moment is

$$p b = \pi a^2 b M \quad (1)$$

$$\text{so} \\ p = \pi a^2 M \quad (2)$$

On the other hand, a uniform magnetization is equivalent¹ to a surface current density (in Gaussian units)

$$\underline{J} = c(\underline{M} \times \underline{n}) \quad (3)$$

where \underline{n} is a unit vector normal to the surface. This expression vanishes on the ends of the magnet, so we are left with a cylindrical sheet current, quite similar to that in a solenoid. The magnetic field on axis, in vacuum at the end of a solenoid of radius a and length b , is

$$\begin{aligned} H &= \frac{2\pi J}{c} \quad b/(a^2 + b^2)^{1/2} \\ &= 2\pi M \quad b/(a^2 + b^2)^{1/2} \end{aligned} \quad (4)$$

From (2),

$$p = (H/2)a^2(1 + (a/b)^2)^{1/2} \quad (5)$$

The rotor magnets have $b = 3.6$ cm and $a = 0.75$ cm so, in Gaussian units,

The rotor contains 8 such poles, of strength $\pm p$. To specify their position, set up a cylindrical coordinate system (z, r, θ) , with origin at the mounting plate and z-axis along the axis of the shielding can. The direction $\theta = 0$ is along the axis of the rotor from the intersection with the z-axis at $z = z_j$.

The explicit values of the coordinates (z_j, r_j, θ_j) of the 8 poles are given in Table 11. Here $h = 1.45$ cm is the distance from the z-axis to the plane of the nearer poles, and $d = 1.45$ cm is the distance of each pole from the rotor axis. The coordinates of course vary as the rotor rotates. Note that the poles are numbered so that negative poles are odd. Poles 1 to 4 are those nearest the z-axis.

Field Inside Shielding Can

The scalar potential inside a cylindrical equipotential can of length L and radius R , due to a point pole of strength p at (z_j, r_j, θ_j) , is calculated in standard texts¹. It is given by

$$\phi_j = \frac{4p}{R} \sum_{m=-\infty}^{\infty} \sum_{n=1}^{\infty} \frac{\exp(im(\theta - \theta_j)) J_m(x_{mn} r/R) J_m(x_{mn} r_j/R)}{x_{mn} J_{m+1}^2(x_{mn}) \sinh(x_{mn} L/R)} \\ \times \sinh(x_{mn} z_{j<}/R) \sinh(x_{mn} (L - z_{j>})/R) \quad (7)$$

In this expression, x_{mn} is the n th root of the Bessel function $J_m(x)$, and $z_{j<} (z_{j>})$ is the smaller (larger) of z and z_j .

In the present case, there are eight poles, and the total potential is

$$\begin{aligned}
\phi &= \sum_{j=1}^8 (-1)^j \phi_j \\
&= \frac{4p}{R} \sum_{j=1}^8 (-1)^j \sum_{m=-\infty}^{\infty} \sum_{n=1}^{\infty} \frac{\exp(im(\theta - \theta_j)) J_m(x_{mn} r/R) J_m(x_{mn} r_j/R)}{x_{mn} J_{m+1}^2(x_{mn}) \sinh(x_{mn} L/R)} \\
&\quad \times \sinh(x_{mn} z_{j<}/R) \sinh(x_{mn} (L - z_{j>})/R) \quad (8)
\end{aligned}$$

The magnetic field is

$$\underline{H} = -\nabla \phi \quad (9)$$

Eq.(8) may be differentiated to give the field anywhere inside the can. However, since we are interested only in the approximate magnitude of the field, we restrict attention to the simplest and most important area, at the mounting plate. Near this surface, $z_{j<} = z$, $z_{j>} = z_j$. The field is axial and is given by

$$\begin{aligned}
H &= - \left. \frac{\partial \phi}{\partial z} \right|_{z=0} \\
&= \frac{4p}{R} \sum_{j=1}^8 (-1)^j \sum_{m=-\infty}^{\infty} \sum_{n=1}^{\infty} \frac{\exp(im(\theta - \theta_j)) J_m(x_{mn} r/R) J_m(x_{mn} r_j/R)}{J_{m+1}^2(x_{mn}) \sinh(x_{mn} L/R)} \\
&\quad \times \sinh(x_{mn} (L - z_j)/R) \quad (10)
\end{aligned}$$

For computational purposes, (10) may be given a more convenient form by noting that, with m an integer,

$$J_{-m}(x) = (-1)^m J_m(x) \quad (11)$$

The roots of $J_{-m}(x)$ are thus the same as those of $J_m(x)$. Using the recurrence relation for Bessel functions, we find

$$\begin{aligned} J_{-m+1}^2(x_{mn}) &= (-1)^{2(m-1)} J_{m-1}^2(x_{mn}) \\ &= \left[\frac{2m}{x_{mn}} J_m(x_{mn}) - J_{m+1}(x_{mn}) \right]^2 \\ &= J_{m+1}^2(x_{mn}) \end{aligned} \quad (12)$$

since $J_m(x_{mn}) = 0$, by definition.

With (11) and (12), (10) may be written

$$\begin{aligned} H &= \frac{4p}{R^2} \sum_{j=1}^8 (-1)^j \sum_{n=1}^{\infty} \sum_{m=0}^{\infty} \frac{c_m \cos m(\theta - \theta_j) J_m(x_{mn} r/R) J_m(x_{mn} r_j/R)}{J_{m+1}(x_{mn})} \\ &\quad \times \frac{\sinh(x_{mn}(L-z_j)/R)}{\sinh(x_{mn}L/R)} \end{aligned} \quad (13)$$

where

$$\begin{aligned} c_m &= 1 & \text{if } m = 0 \\ &= 2 & \text{if } m > 0 \end{aligned} \quad (14)$$

It was noted previously that the pole configuration repeats every π radians as the rotor rotates, so that the fundamental term in (13) is at twice the rotor frequency. The amplitude of this term (and of the harmonics) could in principle be obtained by Fourier analysis of (13), but the integrals involved are complicated. To obtain an estimate of the

fields, we therefore specialize the calculation further, to that of the fields along $\theta = 0$ and $\theta = \pi$.

Rotation of the rotor by $\pi/2$ radians is equivalent to reversing the sign of each pole - i.e., to changing the sign of p in (12). The fields thus reverse every $\pi/2$ radians.

Note that

$$\begin{aligned} \cos m(\theta - \theta_j) &= \cos m\theta_j & \text{if } \theta &= 0 \\ &= (-1)^m \cos m\theta_j & \text{if } \theta &= \pi \end{aligned} \quad (15)$$

The sum over j in (13) is now

$$\sum_{j=1}^8 (-1)^j \cos m\theta_j J_m(x_{mn} r_j / R) \sinh((L - z_j) / R) \quad (16)$$

At the instant when $\omega t = \pi/4$, the pole pairs are symmetric with respect to the plane through the z -axis and $\theta = 0$, which suggests that the fields along the line $\theta = 0$ (or $\theta = \pi$) on the base plate vanish at this time. This is confirmed by inserting the pole coordinates from Table II in (16).

Since the fields vanish at $\omega t = \pi/4$, and since they reverse every $\pi/2$ radians, the amplitude of the field may be calculated by taking $\omega t = 0$ in (13). After some reduction, we obtain

$$\begin{aligned}
u &= \frac{\delta p}{R^3} \sum_{m=0}^{\infty} \sum_{n=1}^{\infty} \frac{c'_m J_m(x_{mn} r/R) \sinh(x_{mn}(L-z_r)/R)}{J_{m+1}^2(x_{mn}) \sinh(x_{mn} L/R)} \\
&= [J_m(x_{mn}(h^2+d^2)^{1/2}/R) \cos m\alpha - J_m(x_{mn}(h^2+d^2+b^2)^{1/2}/R) \cos m\alpha' \\
&\quad + (J_m(x_{mn}(h+b)/R) - J_m(x_{mn} h/R)) \cosh(d/R)] \quad (17)
\end{aligned}$$

where

$$\alpha = \tan^{-1}(d/H)$$

$$\alpha' = \tan^{-1}(d/(h+b))$$

$$\begin{aligned}
c'_m &= 1 && \text{if } m = 0 \text{ and } \theta = 0 \text{ or } \pi \\
&= 2(-1)^m && \text{if } m > 0 \text{ and } \theta = \pi \\
&= 2 && \text{if } m > 0 \text{ and } \theta = 0
\end{aligned} \quad (18)$$

In order to use (17) for calculation, the values of the roots x_{mn} are needed. A first approximation is given by the asymptotic formula

$$x_{mn} = n\pi + (2m-1)\pi/4 \quad (19)$$

Better approximations may be found by using Newton's method for solution of $J_m(x) = 0$. First note that

$$\frac{d}{dx} J_m(x) = \frac{m}{x} J_m(x) - J_{m+1}(x) \quad (20)$$

If x_k is an approximation to the root, a better one is $x_k + \Delta_k$, where

$$A_k = -J_m(x_k) / \left(\frac{m}{x_k} J_m(x_k) - J_{m+1}(x_k) \right) \quad (21)$$

The Bessel functions are calculated from the series

$$J_m(x) = \sum_{i=0}^{\infty} \frac{(-1)^i}{i!(i+m)!} (x/2)^{2i+m} \quad (22)$$

These relations were used to compute the amplitude of the magnetic field along the line $\theta = 0$ from $-R$ to R on the base plate. The results are shown in Figure 11. The maximum field is 6.8 gauss, and the field at the location of the displacer hole is 5.9 gauss. As one would expect, the peak field is displaced slightly from the centerline, because of the asymmetric positions of the rotor poles.

Can shielding Factors

In order to estimate the shielding afforded by the cans, we consider a region containing a uniform induction B_{ext} . A can made from material of permeability μ is now placed in this region, and the internal field B_{int} is calculated. The shielding factor is defined as

$$S = B_{ext}/B_{int} \quad (23)$$

A solution to this problem is available¹ for the case of a spherical shell, of inner and outer radii R_1 and R_2 . For $\mu \gg 1$, the result is

$$S = \frac{2\mu}{9} (1 - (R_1/R_2)^3) \quad (24)$$

If the shell thickness is $d \ll R$, this reduces to

$$S = 2\mu d/3R_1 \quad (25)$$

In order to estimate the shielding in the proposed refrigerator design, it is necessary to determine (i) whether the shielding factor depends strongly on the shape of the can; and (ii) the effects of multiple shields. These questions may be answered by considering an assembly of n infinitely long, concentric cylindrical cans, each of thickness d , with a spacing x between successive shields. A crosssection through an assembly of this type is shown in Figure 12.

The inner and outer radii of the cans are R_j , with $j = 1, 2, \dots, 2n$. The radius of the shielded space in the center is R_1 , and the inner and outer radius of the k^{th} can are R_{2k-1} and R_{2k} . From inspection of the figure, it is easy to see that

$$\begin{aligned} r_j &= r_1 + (j-1)(x+d)/2 & j \text{ odd (inner radius of a can)} \\ r_j &= r_1 + (j-1)(x+d)/2 + (d-x)/2 & j \text{ even (outer radius)} \end{aligned} \quad (26)$$

The regions shown in the figure are also numbered consecutively, with 0 representing the central region. Odd-numbered regions consist of shielding material, and even-numbered regions are spaces. The permeability of the j^{th} region is thus

$$\begin{aligned} \nu_j &= \mu & (j \text{ odd}) \\ &= 1 & (j \text{ even}) \end{aligned} \quad (27)$$

Note that, for all j ,

$$\begin{aligned} \nu_j + \nu_{j-1} &= \mu + 1 \\ \nu_j - \nu_{j-1} &= -(-1)^j(\mu-1) \end{aligned} \quad (28)$$

The shield assembly is placed in a region which initially contained a uniform induction $\underline{B}_{\text{ext}}$.

Since there are no poles present, the potential satisfies Laplace's equation everywhere. There is no variation with axial distance, so the equation is

$$\frac{\partial^2 \phi}{\partial r^2} + \frac{1}{r} \frac{\partial \phi}{\partial r} + \frac{1}{r^2} \frac{\partial^2 \phi}{\partial \theta^2} = 0 \quad (29)$$

This equation may be readily solved by separation of variables. The potential in the j^{th} region is found to be

$$\phi_j = \sum_{m=0}^{\infty} (B_{jm} r^m + C_{jm} r^{-m}) (\cos m\theta + D_{jm} \sin m\theta) \quad (30)$$

where the constants B_{jm} , C_{jm} , and D_{jm} are to be determined from the boundary conditions.

In the region outside the can ($j=2n$), at great distances the induction must reduce to the constant $\underline{B}_{\text{ext}}$. This implies that

$$\phi_{2n} = -B_{\text{ext}} r \cos \theta + \sum_{m=0}^{\infty} C_{2n,m} r^{-m} (\cos m\theta + D_{2n,m} \sin m\theta) \quad (31)$$

where θ is the angle away from the direction of $-B_{\text{ext}}$.

The potential in the central region must not be infinite on axis, so that

$$\phi_0 = \sum_{m=0}^{\infty} B_{0m} r^m (\cos m\theta + D_{0m} \sin m\theta) \quad (32)$$

The boundary conditions at the inner and outer surface of the cans are⁵ that the tangential components of the field and the radial components of the induction are continuous. This means

$$\left. \frac{\partial \phi_j}{\partial \theta} \right|_{r=R_j} = \left. \frac{\partial \phi_{j-1}}{\partial \theta} \right|_{r=R_j} \quad (j = 1 \text{ to } 2n) \quad (33)$$

and

$$\mu_j \left. \frac{\partial \phi_j}{\partial r} \right|_{r=R_j} = \mu_{j-1} \left. \frac{\partial \phi_{j-1}}{\partial r} \right|_{r=R_j} \quad (j = 1 \text{ to } 2n) \quad (34)$$

When (30) is used in these expressions, it is found that matching (31) requires that $D_{jm} = 0$ for all m and that $B_{jm} = C_{jm} = 0$ if $m \neq 1$. The summations may thus be dropped, and the potential in the j^{th} region can be written

$$\Phi_j = (B_j r + C_j r^{-1}) \cos \theta \quad (35)$$

with

$$\Phi_{2n} = -B_{\text{ext}} r \cos \theta + C_{2n} r^{-1} \cos \theta \quad (36)$$

$$\Phi_0 = B_0 r \cos \theta \quad (37)$$

Since $B_{2n} = -B_{\text{ext}}$ and $B_{\text{int}} = -B_0$, the shielding factor for n cans is

$$S_n = B_{\text{ext}}/B_{\text{int}} = B_{2n}/B_0 \quad (38)$$

The boundary conditions (33) and (34) provide $4n$ relations amongst the coefficients B_j and C_j . Fortunately, the form of these relations permits a much easier solution procedure than inverting a $4n \times 4n$ matrix. When (35) is used in the boundary conditions, we obtain

$$B_j R_j + C_j R_j^{-1} = B_{j-1} R_j + C_{j-1} R_j^{-1} \quad (39)$$

$$\mu_j (B_j - C_j R_j^{-2}) = \mu_{j-1} (B_{j-1} - C_{j-1} R_j^{-2}) \quad (40)$$

Using (28), these equations may be solved, to give the recurrence relations

$$B_j = [(\mu+1)B_{j-1} - (-1)^j (\mu-1) R_j^{-2} C_{j-1}] / 2\mu_j \quad (41)$$

$$C_j = - [(-1)^j (\mu-1) R_j^2 B_{j-1} - (\mu+1) C_{j-1}] / 2\mu_j \quad (42)$$

According to (37), $C_0 = 0$, so the first few of these relations yield

$$B_1 = \frac{\mu+1}{2\mu} B_0 \quad (43)$$

$$C_1 = \frac{\mu-1}{2\mu} R_1^2 B_0 \quad (44)$$

$$B_2 = \frac{1}{4\mu} [(\mu+1)^2 - (\mu-1)^2 (R_1/R_2)^2] B_0 \quad (45)$$

$$C_2 = - \frac{(\mu^2-1)}{4\mu} (R_2^2 - R_1^2) B_0 \quad (46)$$

For a single cylindrical shield, (38) gives the shielding factor as

$$\begin{aligned} S_1 = B_2/B_0 &= \frac{1}{4\mu} [(\mu+1)^2 - (\mu-1)^2 (R_1/R_2)^2] \\ &= \frac{\mu}{4} (1 - (R_1/R_2)^2) \quad \text{for } \mu \gg 1 \end{aligned} \quad (47)$$

Since $R_2 = R_1 + d$, we obtain, for $d \ll R_1$,

$$S_1 = \mu d / 4R_1 \quad (48)$$

Comparison with (25) shows that a thin spherical shield provides slightly greater shielding than a long cylindrical shield of the same material, radius and thickness. The ratio is however only 4/3, so that the effects of shield geometry are negligible. For the actual shield can shape, it is expected that an accurate calculation would lead to a result between (48) and (25).

Continuation of the progression (43) to (46), for multiple shields, leads to expressions of rapidly increasing algebraic complexity. The labor involved in deriving these expressions is, however, superfluous because the recurrence relations (41) and (42) can be used directly for a numerical calculation of the shielding factor for any number of shields.

As one would expect, the coefficients B_j and C_j are all proportional to B_0 : this simply reflects the fact that, in the present approximation (μ independent of field strength), the shielding factor is independent of B_{ext} . It is therefore possible to put $B_0=1$ in the calculation, so that, numerically, $S_n=B_{2n}$. Starting with the values for B_1 and C_1 from (43) and (44), the successive effects of additional shields can be obtained numerically, using the recurrence relations.

It is also possible to provide results applicable to any cylindrical shield assembly by normalizing the shield thickness and spacing to the radius $R_1=1$ in (26).

In order to carry out these calculations, it is of course necessary to specify μ . The manufacturer's test procedure for HyMu "80" material involves measurement of the shielding factor (attenuation) of a single cylindrical shield in an initially constant external field. The measured values of S_1 range from about 100 to more than 600, depending on the thickness of the shield, the magnitude of the external field, and the annealing temperature of the shield. Using the test shield dimensions in (48) gives permeability values ranging from 30,000 to 165,000.

In the refrigerator under study, the shield thickness, divided by the inner shield radius, is expected to be about 0.005. With this value, (41) and (42) were used to calculate the shielding factors for one to four shields, as a function of the normalized spacing between them. The results are shown in Figure 3, for $\mu = 30,000$ and $\mu = 100,000$.

Estimation of Fields at the End of the Cold Finger

o Leakage from Displacer Hole

The field at the baseplate at the location of the displacer hole was estimated previously as 5.9 gauss. The actual field at the displacer hole will be distorted by the hole itself and by the surrounding structure. The hole radius is approximately 1 cm, and it is proposed to surround it by a collar of high permeability material, 0.5 cm thick, extending up into the shield can for a distance of 7 cm.

Application of (47) to this collar gives a shield factor of 1300 if its permeability is 10^4 . The field in the hole is therefore expected to be a few milligauss.

Accurate extrapolation of this field to that at the end of the cold finger would require detailed knowledge of the field distribution in the hole. A good rule of thumb is however that the field will be reduced in the far field, at a distance r , by the cube of the ratio of the hole radius to this distance. Since the end of the cold finger is at a distance of 22 cm, this factor should be of order 10^4 .

The conclusion is thus that the magnetic signature due to leakage through the displacer hole will be a few times 10^{-7} gauss, within specifications.

o Leakage Through Cylindrical Shields

The radius of the outer shield can is 12 cm. The inverse cube decrease in field strength provides a less satisfactory rule of thumb for extrapolating leakage fields through the can to the end of the cold finger in this case, because the dimensions of the can are such that the cold finger cannot be regarded as truly in the far field. It is doubtful

that the distance effect will reduce these fields by more than a factor of 5.

Since the interior fields are of order 5 gauss, meeting a microgauss specification at the cold finger requires a shield factor of order 10^6 . The normalized spacing between shields is ≈ 0.1 . Inspection of Figure 13 shows that performance will be marginal with 3 shields for $\mu = 10^5$ or 4 shields for $\mu = 3 \times 10^4$. If a permeability approaching 10^5 can be achieved, 4 shields should however be more than adequate.

TABLE 11
COORDINATES OF THE ROTOR POLES

Pole #	Sign	z_j	r_j	θ_j
1	-	$z_r + d \cos \omega t$	$(h^2 + d^2 \sin^2 \omega t)^{1/2}$	$\tan^{-1}(\frac{d}{h} \sin \omega t)$
2	+	$z_r - d \sin \omega t$	$(h^2 + d^2 \cos^2 \omega t)^{1/2}$	$\tan^{-1}(\frac{d}{h} \cos \omega t)$
3	-	$z_r - d \cos \omega t$	$(h^2 + d^2 \sin^2 \omega t)^{1/2}$	$-\tan^{-1}(\frac{d}{h} \sin \omega t)$
4	+	$z_r + d \sin \omega t$	$(h^2 + d^2 \cos^2 \omega t)^{1/2}$	$-\tan^{-1}(\frac{d}{h} \cos \omega t)$
5	-	$z_r + d \sin \omega t$	$((h+b)^2 + d^2 \cos^2 \omega t)^{1/2}$	$-\tan^{-1}(\frac{d}{h+b} \cos \omega t)$
6	+	$z_r + d \cos \omega t$	$((h+b)^2 + d^2 \sin^2 \omega t)^{1/2}$	$\tan^{-1}(\frac{d}{h+b} \sin \omega t)$
7	-	$z_r - d \sin \omega t$	$((h+b)^2 + d^2 \cos^2 \omega t)^{1/2}$	$\tan^{-1}(\frac{d}{h+b} \cos \omega t)$
8	+	$z_r - d \cos \omega t$	$((h+b)^2 + d^2 \sin^2 \omega t)^{1/2}$	$-\tan^{-1}(\frac{d}{h+b} \sin \omega t)$

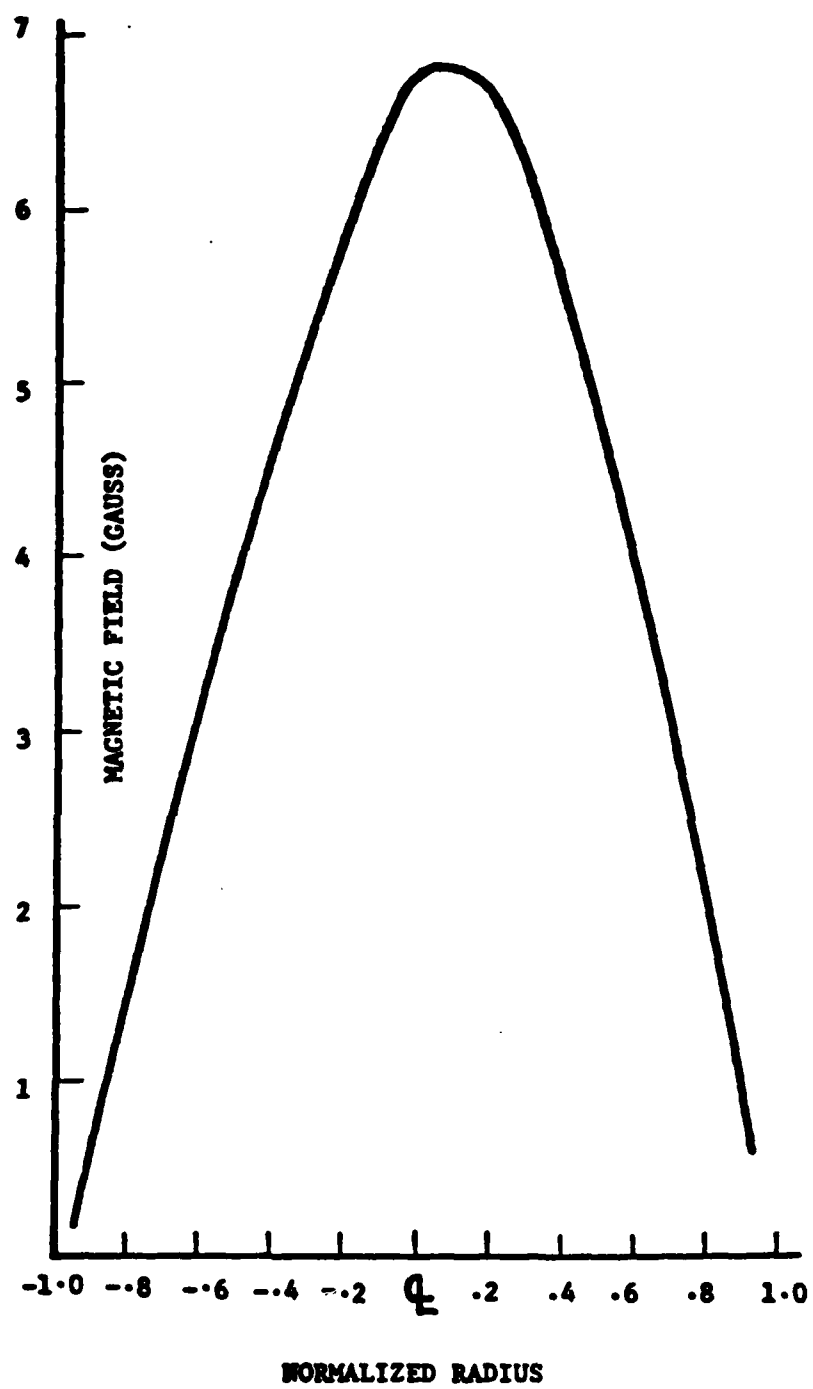
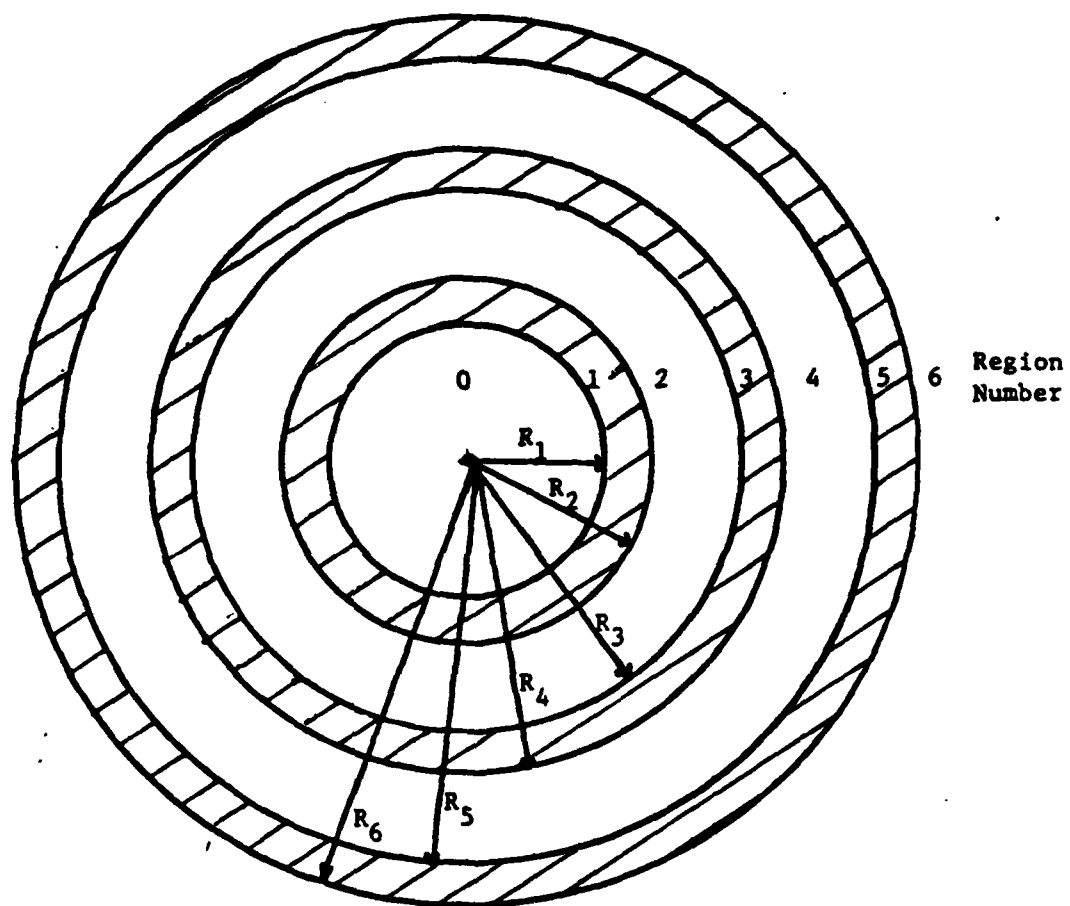


Figure 11: Field At Baseplate



Shield Thickness: d

Shield Spacing: x

Figure 12. Concentric Shield Assembly

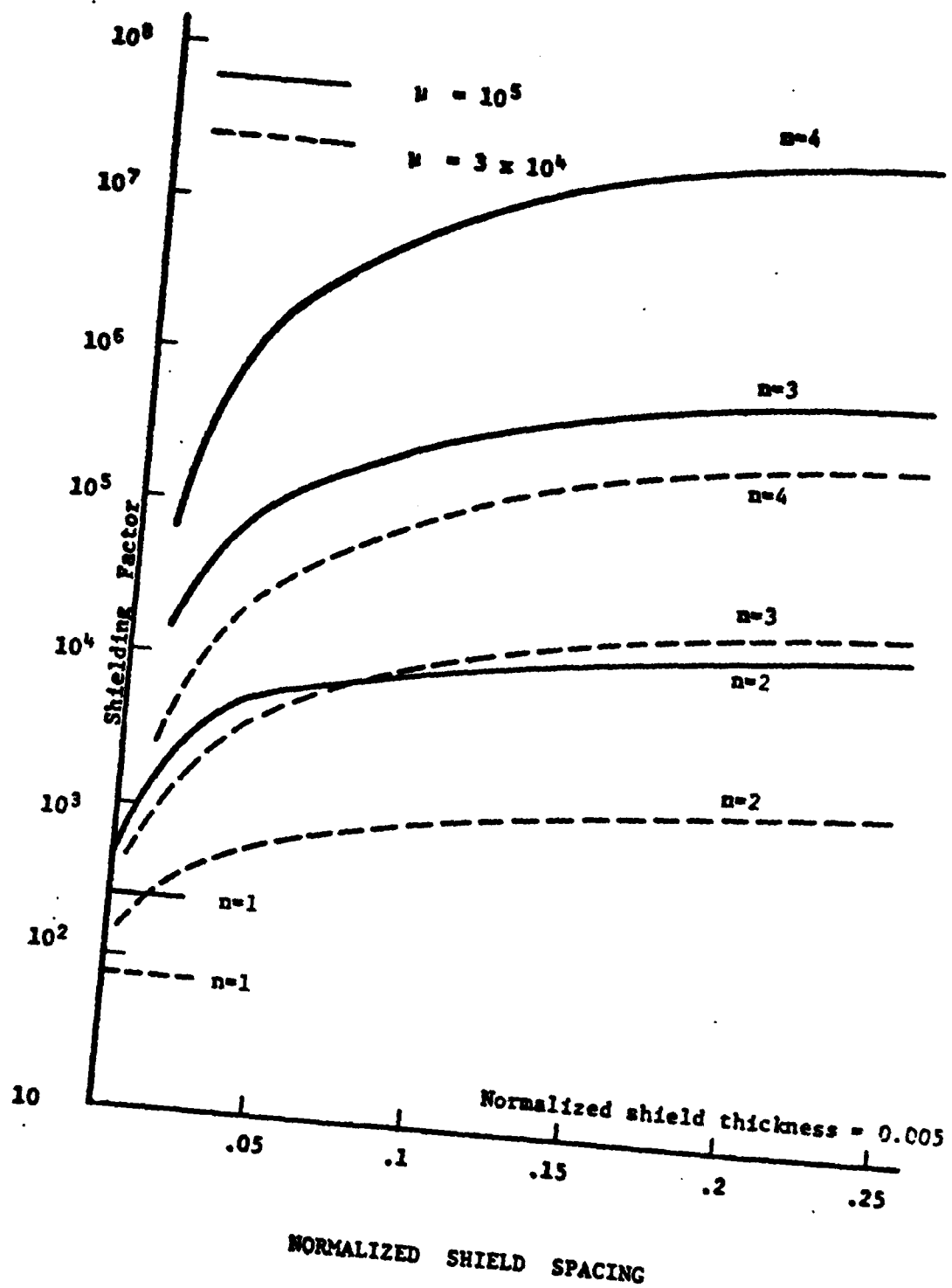


Figure 13: Shield Effectiveness

REFERENCES

1. Jackson, J.D., Classical Electrodynamics, Wiley (1962)
2. Dushman, S, Scientific Foundations of Vacuum Technique, Second Edition, Wiley

DATE
FILMED
-8